

San Jose State University

From the Selected Works of Thomas P. Connolly

January, 2014

Coastal Trapped Waves, Alongshore Pressure Gradients, and the California Undercurrent

Thomas P. Connolly, *Woods Hole Oceanographic Institution*

Barbara M. Hickey, *University of Washington*

Igor Shulman, *Stennis Space Center*

Richard E. Thomson, *Institute of Ocean Sciences*



Available at: <https://works.bepress.com/thomas-connolly/3/>

Coastal Trapped Waves, Alongshore Pressure Gradients, and the California Undercurrent*

THOMAS P. CONNOLLY

Woods Hole Oceanographic Institution, Woods Hole, Massachusetts

BARBARA M. HICKEY

University of Washington, Seattle, Washington

IGOR SHULMAN

Naval Research Laboratory, Stennis Space Center, Mississippi

RICHARD E. THOMSON

Institute of Ocean Sciences, Sidney, British Columbia, Canada

(Manuscript received 30 April 2013, in final form 23 September 2013)

ABSTRACT

The California Undercurrent (CUC), a poleward-flowing feature over the continental slope, is a key transport pathway along the west coast of North America and an important component of regional upwelling dynamics. This study examines the poleward undercurrent and alongshore pressure gradients in the northern California Current System (CCS), where local wind stress forcing is relatively weak. The dynamics of the undercurrent are compared in the primitive equation Navy Coastal Ocean Model and a linear coastal trapped wave model. Both models are validated using hydrographic data and current-meter observations in the core of the undercurrent in the northern CCS. In the linear model, variability in the predominantly equatorward wind stress along the U.S. West Coast produces episodic reversals to poleward flow over the northern CCS slope during summer. However, reproducing the persistence of the undercurrent during late summer requires additional incoming energy from sea level variability applied south of the region of the strongest wind forcing. The relative importance of the barotropic and baroclinic components of the modeled alongshore pressure gradient changes with latitude. In contrast to the southern and central portions of the CCS, the baroclinic component of the alongshore pressure gradient provides the primary poleward force at CUC depths over the northern CCS slope. At time scales from weeks to months, the alongshore pressure gradient force is primarily balanced by the Coriolis force associated with onshore flow.

1. Introduction

The California Undercurrent (CUC) flows poleward over the continental slope along the eastern boundary of

the North Pacific Ocean, transporting heat, chemical tracers, and organisms over alongshore distances of thousands of kilometers. Relatively warm, saline, and oxygen-depleted water is associated with the CUC from Baja California to Alaska (Hickey 1979; Thomson and Krassovski 2010). These equatorial water properties are transferred into the interior of the North Pacific by eddies formed from instabilities within the CUC (Huyer et al. 1998; Garfield et al. 1999). The CUC modifies nutrient concentrations along its path by transporting water with low ratios of nitrate to phosphate (Liu and Kaplan 1989; Castro et al. 2001) and also influences the distribution of marine organisms such as zooplankton (Swartzman et al. 2005). Poleward undercurrents similar

*Ecology and Oceanography of Harmful Algal Blooms (ECOHAB) Contribution Number 769, ECOHAB Pacific Northwest Contribution Number 33, and Pacific Northwest Toxin Contribution Number 8.

Corresponding author address: Thomas P. Connolly, Woods Hole Oceanographic Institution, MS 21, 266 Woods Hole Road, Woods Hole, MA 02543-1050.
E-mail: tconnolly@whoi.edu

to the CUC are common in eastern boundary current systems, and their presence can greatly affect the physical dynamics of coastal upwelling (Hill et al. 1998).

The CUC is a seasonal feature in the northern California Current System (CCS; Hickey 1979; Thomson and Krassovski 2010), which includes the coastal waters offshore of northern California (CA), Oregon (OR), Washington (WA), and southern British Columbia (BC). Following Hickey (1979), the CUC is defined as a subsurface maximum in poleward flow over the continental slope and below the main pycnocline. At these latitudes, the CUC has a typical volume transport of 0.5–1.5 Sverdrups (Sv; $1 \text{ Sv} \equiv 10^6 \text{ m}^3 \text{ s}^{-1}$), with a 10–20-km-wide subsurface core over the upper slope (Hickey 1979; Pierce et al. 2000). In the seasonal cycle, poleward flow appears over the upper slope at depths <300 m during July and strengthens through late October (Hickey 1979; Thomson and Krassovski 2010). Lagrangian floats at 250–600-m depth between 40° and 47°N indicate that poleward flow is present year-round but is weakest during March and strongest during October (Collins et al. 2003). As the upwelling season progresses from late April to early October, the core of the undercurrent shoals from below 500-m depth to the upper slope (Pelland et al. 2013), and the relatively warm and saline CUC water mass forms a greater percentage of water over the shelf (MacFadyen et al. 2008). During winter, winds are downwelling favorable, and the CUC merges with the surface-intensified poleward flow over the slope commonly known as the Davidson Current (Hickey 1979). The spring transition to equatorward flow over the upper slope precedes the transition to upwelling-favorable wind stress by around one month (Thomson and Krassovski 2010).

The CUC influences the seasonal dynamics of coastal upwelling in the CCS because of its relationship to the alongshore pressure gradient and the bottom boundary layer. In the northern CCS, the barotropic component of the alongshore pressure gradient force (APF) at the coast is directed equatorward during winter and spring and becomes poleward during the summer upwelling season (Hickey and Pola 1983). Imposing a poleward APF in two-dimensional models of coastal upwelling produces a poleward undercurrent over the slope and shifts the depth of onshore flow from the bottom boundary layer to the interior (Werner and Hickey 1983; Federiuk and Allen 1995). Similarly, Pringle and Dever (2009) found that incorporating a realistic CUC into a three-dimensional regional hindcast model leads to shallower source depths for upwelling. Idealized modeling studies of upwelling ecosystems and biogeochemistry often use an externally applied poleward APF to incorporate undercurrent dynamics (Lathuilière et al. 2010; Siedlecki et al. 2012). However, it is not clear how the structure of the APF varies

in the cross-shore direction or whether there is a baroclinic component associated with large-scale density gradients.

Despite the prevalence and importance of eastern boundary poleward undercurrents like the CUC, mechanisms for their generation are not fully understood. Hill et al. (1998) classify three proposed mechanisms: 1) a response to wind stress near the coast, 2) pressure gradients originating in the open ocean, and 3) rectification of oscillating flow over complex topography. The first two mechanisms depend on a large-scale poleward APF. In idealized wind-driven models with stratification, a poleward APF and undercurrent can be generated if the upwelling-favorable winds have an alongshore structure, an idea first recognized by Yoshida (1967). However, an open-ocean pressure gradient associated with a poleward decrease in temperature and sea surface height (SSH) can also be associated with a poleward flow over the slope (Huthnance 1984; Csanady 1985). In the third mechanism, poleward flow is associated with a mean asymmetrical distribution of pressure across topographic features (Holloway 1987; Brink 2010, 2011). In this case, the oscillating flow may be forced by variable alongshore wind stress, but over the course of many oscillations, mean poleward flow over the slope arises in the absence of a mean wind stress. All of the above mechanisms can produce poleward flow over the slope that qualitatively resembles the cross-shelf and depth structure found in the limited existing observations of the undercurrent, but the different types of forcing should result in differences in the temporal variability of poleward flow. The absence of a clearly defined mechanism for undercurrent generation continues due to the low number of velocity time series characterizing the temporal variability of slope currents and the difficulty in obtaining measurements of the APF.

In the theoretical work that emphasizes wind forcing as a mechanism for undercurrent generation, coastal trapped waves (CTWs) play an important role. CTWs are hybrids of internal Kelvin waves and barotropic continental shelf waves (Wang and Mooers 1976). In pure internal Kelvin waves, over a flat bottom, alongshore pressure gradients accelerate alongshore motions near a coastal wall but cross-shore velocity remains zero. In shelf waves, cross-shore motions act to conserve potential vorticity over a sloping bottom. When stratification and bottom slope are present, CTWs are nearly barotropic over the shelf, with a more baroclinic structure over the slope. Higher modes tend to have more baroclinic structure than lower modes, are damped more rapidly by friction, and propagate more slowly.

The undercurrent is a robust feature of models forced by wind stress in a region of limited alongshore extent. In stratified models with a flat bottom, Kelvin waves are generated at the southern edge of the forcing region, and

a poleward APF that accelerates the undercurrent is set up in their wake (McCreary 1981; Philander and Yoon 1982). When a continental shelf is present, the first-mode CTW is associated with equatorward flow, and a poleward flow develops over the slope with the passage of a second-mode CTW (Suginohara 1974, 1982).

The two essential ingredients for wind-driven poleward undercurrents are alongshore structure in the wind forcing, which generates an APF, and stratification, which allows vertical shear in the alongshore currents. With these basic factors included, the two-layer analytical model of Yoshida (1980) produces a poleward undercurrent over nearly the entire range of length scales and frequencies. The β effect is not essential for modeling the undercurrent, but offshore Rossby wave propagation can lead to a shallowing and intensification of the undercurrent (Suginohara and Kitamura 1984; McCreary and Chao 1985; Marchesiello et al. 2003). Positive wind stress curl near the coast on a β plane can also strengthen the undercurrent (McCreary and Chao 1985; Batteen 1997).

The timing of CUC development in the northern CCS, shown by Thomson and Krassovski (2010), is qualitatively consistent with a summertime poleward APF inferred from coastal sea level observations (Hickey and Pola 1983). Hickey and Pola (1983) attributed the sea level gradient in the northern CCS to the alongshore structure of wind stress using the steady barotropic model of Csanady (1978). This structure in summer wind stress, with a maximum off of northern CA, has been linked to the CUC and poleward APF in the baroclinic models (e.g., McCreary 1981) described above. However, direct comparisons with observed variability in the CUC have been limited, making it difficult to rule out other mechanisms of producing poleward flow. Furthermore, because the APF is difficult to measure away from the coast, its structure and variability over the slope remain poorly understood.

The goals of this paper are to investigate the spatial and temporal structure of the poleward undercurrent and the alongshore pressure gradient along the U.S. West Coast, extending previous work by incorporating realistic wind forcing and boundary conditions at time scales from weather events to seasons. Emphasis is placed on the development of the CUC in the northern portion of the CCS, where local wind stress forcing is relatively weak. The analysis uses two numerical hindcasts with different levels of complexity. The Navy Coastal Ocean Model of the CCS (NCOM-CCS) is used to more fully understand the APF over the continental slope, where it is difficult to observe. A linear CTW model is also used, which is forced by temporally and spatially variable winds along the coast but excludes the effects of complex topography, open-ocean forcing, wind

stress curl, and the β effect. These limitations are less restrictive in the northern CCS than at locations farther south because the region lies north of latitudes where seasonal Rossby wave propagation occurs (Clarke and Shi 1991; Kelly et al. 1993) and wind stress curl is relatively weak (Bakun and Nelson 1991). This model can be directly compared with observations and includes the basic ingredients in wind-driven theories of undercurrent generation: alongshore structure in wind stress, alongshore pressure gradients, and stratification. The more complete physics of NCOM-CCS provide our best estimate of the ocean state at locations where observations are limited, while the CTW model is used to isolate the linear response to alongshore wind stress in the CCS.

Both models are compared with an extensive array of observations, including currents from moored sensors and hydrographic data (section 3). The CTW model is adjusted to show the sensitivity of the alongshore velocity to friction, number of modes, local wind stress, and the southern boundary condition (section 4a). In this linear model, alongshore winds along the U.S. West Coast generate episodic periods of poleward flow over the northern CCS slope during summer, when wind-driven flow over the shelf is predominantly equatorward. However, the inclusion of sea level data at the southern boundary, >1500 km to the south, is required to reproduce the observed strength and persistence of the slope undercurrent during late summer. The APF is examined near the coast and over the slope in both models (section 4b), then connected to the dynamics of CUC development through the analysis of the alongshore momentum balance (section 4c). It is shown that alongshore density gradients contribute to a poleward APF over the northern CCS slope, in contrast to locations farther south.

2. Methods

a. Observations

1) COASTAL SEA LEVEL

Coastal sea level time series were obtained for 10 tide gauge locations (Fig. 1a). Sea level data were adjusted by adding equivalent sea level pressure (0.01 m mbar^{-1} atmospheric pressure) measured at nearby stations (Fig. 1a) in order to estimate subsurface pressure. Hourly time series were low-pass filtered using a cosine Lanczos filter with a half-power point of 46 h and decimated every 6 h. Because the absolute vertical displacement from a geopotential surface is unknown, mean values are removed so that time series represent anomalies. Tide gauge data were obtained from the U.S. National Ocean Service, and atmospheric pressure data were obtained from the National Buoy Data Center.

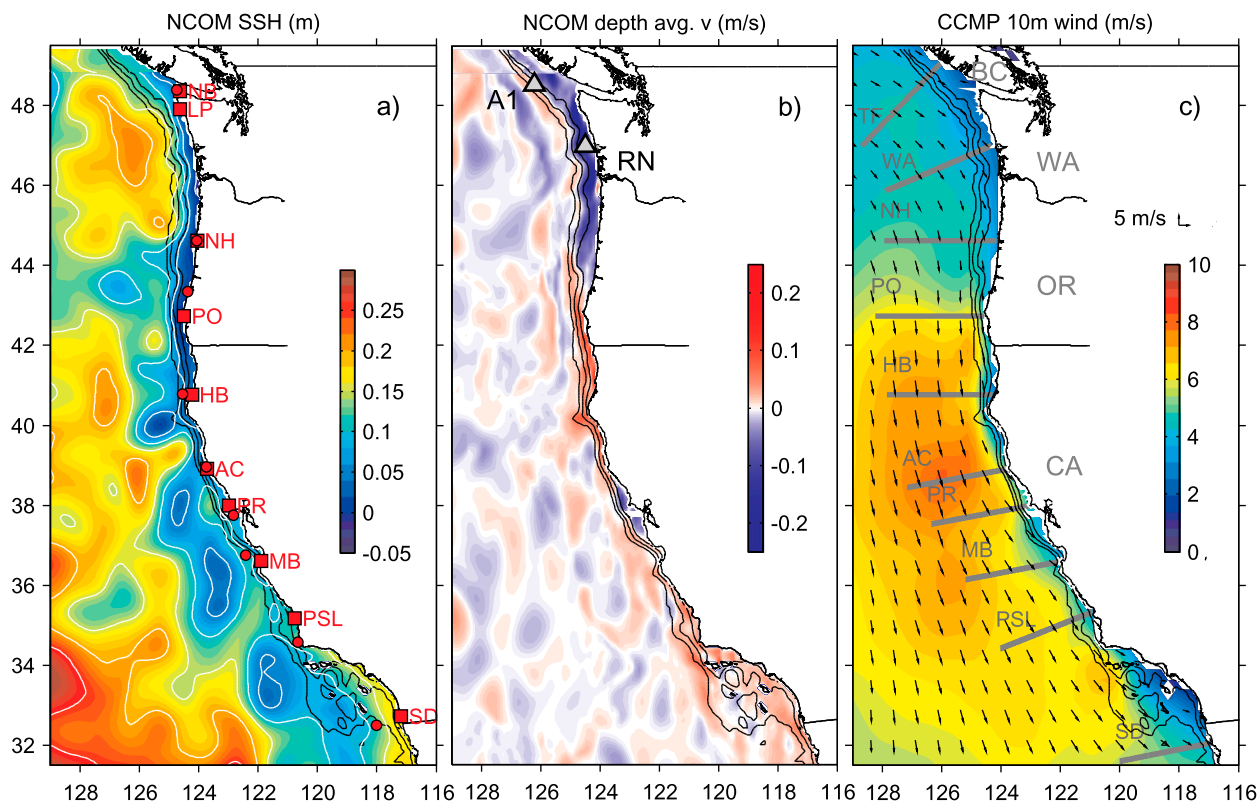


FIG. 1. Mean model fields (NCOM-CCS, with global NCOM north of 49°N) and atmospheric forcing (CCMP) for the California Current, 15 Jun–15 Sep 2005. The 200-, 500-, and 1000-m isobaths are shown as black contours. (a) SSH, with 0.05-m contour intervals in white. Red squares indicate tide gauges at San Diego (SD), Port San Luis (PSL), Monterey Bay (MB), Point Reyes (PR), Arena Cove (AC), Humboldt Bay (HB), Newport (NH), La Push (LP), and Neah Bay (NB). Red circles show nearby measurements of sea level pressure. (b) Northward component of depth-averaged velocity. Gray triangles indicate mooring locations. (c) Wind speed and velocity vectors. Gray lines indicate cross-shore segments used in the coastal trapped wave model. CTW model segments coincide with tide gauge locations at the coast, except for the WA and Tofino (TF) segments. Geographic boundaries of BC, WA, OR, and CA are indicated.

2) MOORING TIME SERIES

Velocity data are used from two locations, one on the British Columbia slope and one on the Washington shelf (Fig. 1b). The A1 mooring, where data have been collected from 1985 through the present, is located on the 500-m isobath at 48°32'N, 126°12'W (Thomson and Krassovski 2010). During 2004 and 2005, velocity data were collected at nominal depths of 35, 100, 175, and 300 m using Aanderaa recording current meters (RCM) 8, although actual current-meter depth and data availability vary between deployments. Velocity components were rotated 25° counterclockwise, parallel to the local isobath orientation, and time series were filtered using a Kaiser-Bessel low-pass filter with a 30-h cutoff and decimated to daily intervals. On the Washington shelf, maintained as part of the River Influences on Shelf Ecosystems (RISE) project (Hickey et al. 2010), the RISE North (RN) mooring is located on the 70-m isobath at 47°00'N, 124°30'W (data provided by E. Dever 2006, personal communication). Velocity components at the RN site

were rotated 10° clockwise, and time series were filtered and decimated in the same manner as coastal sea level.

3) GEOSTROPHIC VELOCITY

Conductivity, temperature, and depth (CTD) measurements were obtained during September 2005 as part of the Ecology and Oceanography of Harmful Algal Blooms Pacific Northwest (ECOHAB-PNW) project (MacFadyen et al. 2008). Geostrophic velocity, referenced to 500 dbar, was calculated using the method of Reid and Mantyla (1976). Because shipboard ADCP data are not available at 500 dbar to compute absolute velocity, NCOM-CCS velocity at 500 dbar is used as a reference for consistent comparison between model and observations.

b. Models

1) NAVY COASTAL OCEAN MODEL

NCOM-CCS (Shulman et al. 2007) is a primitive equation, 3D, hydrostatic model with a horizontal resolution of

~9 km. The model domain covers the region 30°–49°N, 135°–115°W (Figs. 1a,b), and hindcast results are presented for the year 2005. The model is forced with atmospheric products derived from the Coupled Ocean–Atmosphere Mesoscale Prediction System (COAMPS; Hodur 1997). The model assimilates satellite-derived SSH and sea surface temperature (SST) data via the Modular Ocean Data Assimilation System (MODAS; Fox et al. 2002), which uses the SST and SSH data to generate synthetic temperature and salinity profiles. Open boundary conditions for the regional NCOM-CCS are derived from the global NCOM (Rhodes et al. 2002; Barron et al. 2004), which has a 1/8° horizontal resolution. In the version used here, the vertical coordinate system is composed of 40 levels total, 19 σ (terrain following) levels on top of 21 z (constant depth) levels (Shulman et al. 2007). There is no tidal forcing or river input, and the mouth of the Strait of Juan de Fuca at Neah Bay (NB; Fig. 1a) is closed off by a straight coastline. Use of z levels below 138 m, which is typically shallower than the depth of the shelf break in the CCS, avoids errors in calculation of the pressure gradient that can arise near the steep topography of the continental slope when using σ coordinates (Haney 1991).

2) COASTAL TRAPPED WAVE MODEL

A CTW model is used to further isolate mechanisms for subinertial variability in velocity and sea level along the west coast of North America. Derivation and application of CTW theory are discussed extensively by Clarke and Van Gorder (1986) and will only be summarized briefly here. Time-dependent effects of alongshore wind stress are included in the model, along with rotation, continuous stratification, bottom slope, and weak bottom friction. Wind stress curl and the β effect are neglected. The flow is assumed to be linear and Boussinesq, with gradually varying topography in the alongshore direction.

The coordinate system is aligned such that x is the cross-shore distance from the coast (positive onshore), y is the alongshore position (positive northward), and z is the vertical position (positive upward). The problem is greatly simplified in the long-wave limit, in which cross-shelf scales are assumed to be much shorter than alongshore scales (i.e., $\partial^2/\partial y^2 \ll \partial^2/\partial x^2$), and time scales of variability are assumed to be much longer than the inertial period (i.e., $\partial^2/\partial t^2 \ll f^2$, where f is the Coriolis frequency). Turbulent stresses are restricted to infinitesimally thin boundary layers at the surface and bottom. In terms of pressure, the system can be written as

$$p_{xxt} + f^2(p_{zt}/N^2)_z = 0, \quad (1)$$

where $N(z)$ is the buoyancy frequency of the background state, and p is the deviation of pressure from the background state. Boundary conditions are given by

$$p_z + \frac{N^2}{g}p = 0 \quad \text{at } z=0, \quad (2)$$

$$p_{xt} + \frac{rp_x}{h} + fp_y = \frac{f\tau^y}{h} \quad \text{at } x=0, \quad (3)$$

$$\frac{f^2 p_{zt}}{N^2} + h_x(p_{xt} + fp_y) + (rp_x)_x - h_x r p_{xz} = 0 \quad \text{at } z = -h(x), \quad \text{and} \quad (4)$$

$$p_x = 0 \quad \text{as } x \rightarrow \infty, \quad (5)$$

where $\tau^y(y, t)$ is the alongshore component of wind stress, $h(x, y)$ is bottom depth (assumed to vary gradually in the alongshore direction), r is a linear friction coefficient such that the bottom stress $\tau_b^y = \rho_0 r v$, ρ_0 is a reference density, and v is alongshore velocity. These boundary conditions represent a free surface [(2)], no net cross-shelf transport at the coastal wall [(3)], Ekman transport governed by no normal flow at the bottom [(4)], and coastal trapping [(5)]. Solutions for pressure are separated into orthogonal components,

$$p(x, y, z, t) = \sum_{n=1}^{\infty} F_n(x, z)\phi_n(y, t), \quad (6)$$

where F_n is the frictionless free-wave structure of the n th mode, and ϕ_n is the amplitude of the n th-mode response. The ϕ_n satisfy

$$\phi_{ny} - \frac{1}{c_n}\phi_{nt} + a_{nn}\phi_n + \sum_{\substack{m=1 \\ m \neq n}}^{\infty} a_{nm}\phi_m = b_n\tau^y(y, t), \quad (7)$$

where c_n is the phase speed of the n th mode, b_n is a wind coupling coefficient, a_{nn} is a frictional decay coefficient, and a_{nm} are coefficients for frictional coupling to the m th mode. Numerical methods for calculating the free-wave properties F_n , c_n , b_n , and a_{nm} from mean stratification $N^2(z)$, cross-shore bottom topography $h(x)$, and Coriolis parameter f are described by Brink and Chapman (1987). Versions of the software for the Matrix Laboratory (MATLAB) programming environment were provided by Dr. Kenneth Brink [Woods Hole Oceanographic Institution (WHOI)]. Wind coupling coefficients b_n and frictional coefficients a_{nm} are calculated using the energy-conserving normalization of Brink (1989). Once the free-wave properties are found, solutions to the

coupled equations in (7) can be obtained using the numerical method of characteristics described by Clarke and Van Gorder (1986).

The free-wave parameters were calculated for 10 coastal segments (Fig. 1c). Mean $N^2(z)$ profiles for each segment were computed from CTD data in the World Ocean Database (Boyer et al. 2006), using casts offshore of the 1000-m isobath but no farther than 400-km offshore. Previous studies have shown that varying $N^2(z)$ produces small (<10%) changes in F_n , c_n , and b_n in the long-wave limit but can change a_{nm} by up to 100% (Battisti and Hickey 1984; Chapman 1987). Bottom topography is from the National Geophysical Data Center coastal relief model (<http://www.ngdc.noaa.gov/mgg/coastal/crm.html>). Wind stress was calculated using the formula of Large and Pond (1981) from wind velocity interpolated to the in-shore 50 km of each segment from the Cross-Calibrated Multi-Platform (CCMP) product (Fig. 1c), which incorporates data from the Quick Scatterometer (QuikSCAT) and coastal buoys (Atlas et al. 2011).

To resolve the slowest phase speed in the model (0.39 m s^{-1} for the fourth mode off of southern California), Δy and Δt were set to 2.5 km and 6 h, respectively. The CTW model was run for the years 2003–05, with results from 2003 discarded as spinup. Unless otherwise stated, the infinite sums in (6) and (7) were approximated using four modes. A constant linear friction coefficient $r = 2.5 \times 10^{-4} \text{ m s}^{-1}$ was used for the calculation of a_{nm} . This is equivalent to the value used for the continental slope but less than that used for the shelf by Chapman (1987). At the southern boundary, $\phi_1(0, t) = \rho_0 g \eta / F_1(0, 0)$, and adjusted sea level at San Diego was used for $\eta(t)$. This relationship assumes that the San Diego sea level is dominated by the first mode. Sensitivity to the number of modes, friction coefficient, presence of local wind stress, and the use of sea level data at the southern boundary will be explored.

3. Model validation

Validation with observations is necessary before using the models to extend prior work on the CUC dynamics. The models are first compared with observed time series of alongshore velocity at the RN mooring over the WA midshelf (Fig. 1b), where previous studies have demonstrated the importance of CTW dynamics (Battisti and Hickey 1984). To assess the variability and strength of the modeled CUC, the models are also compared with time series at the A1 mooring over the British Columbia slope (Fig. 1b).

Statistical agreement between the models and observations is quantified using both correlation coefficients (CC) and Willmott skill (WS). Correlation provides a

test for statistically significant agreement at weather-band time scales. CC were calculated from a detrended time series, and significance levels were determined using effective degrees of freedom (Emery and Thomson 2004, p. 260). WS normalizes the mean squared error, which includes bias and differences in variance and trends, allowing for comparisons of skill between different models at multiple observational locations. WS varies between 0 and 1 and is defined as

$$WS = 1 - \frac{\langle (m - o)^2 \rangle}{\langle (|m - \langle o \rangle| + |o - \langle o \rangle|)^2 \rangle}, \quad (8)$$

where m is a modeled variable, o is an observed variable, and the angle brackets denote an average over the series (Willmott 1981).

a. Midshelf

During June–September 2005, observed currents were predominantly equatorward in the middle of the water column over the WA shelf (Fig. 2a), and significant variability was also observed at weather-band (~5 days) time scales (Fig. 2a). Reversals to poleward flow do occur during this period over the WA shelf, becoming more frequent during September. Correlations between NCOM-CCS and observations at RN are similar throughout the water column (CC = 0.68–0.74), while CTW model correlation is strongest in the lower half of the water column (CC = 0.61–0.66) (Fig. 3a). All correlations are significant at the 95% confidence level. A similar increase with depth in the correlation between a CTW model and observations was reported by Chapman (1987) over the California shelf. Profiles of WS from the two different models indicate that the CTW model generally has weaker skill, particularly in the lower part of the water column (Fig. 3a). The CTW model most accurately predicts the timing of fluctuations near the bottom, but the magnitude of the modeled velocity agrees more closely with observations near the surface.

b. Slope

During 2005 at the A1 site on the continental slope, models show greater agreement with observations at undercurrent depths than near the surface (Figs. 2b,c). Observations at 35 m show equatorward flow that intensifies from June to September (Fig. 2b), a pattern that is not shown in either model. At 300-m depth, the strongest equatorward flows were observed during late May, following the transition in local wind stress (Fig. 2c). By mid-July, the flow is predominantly poleward but with considerable event-scale variability throughout the

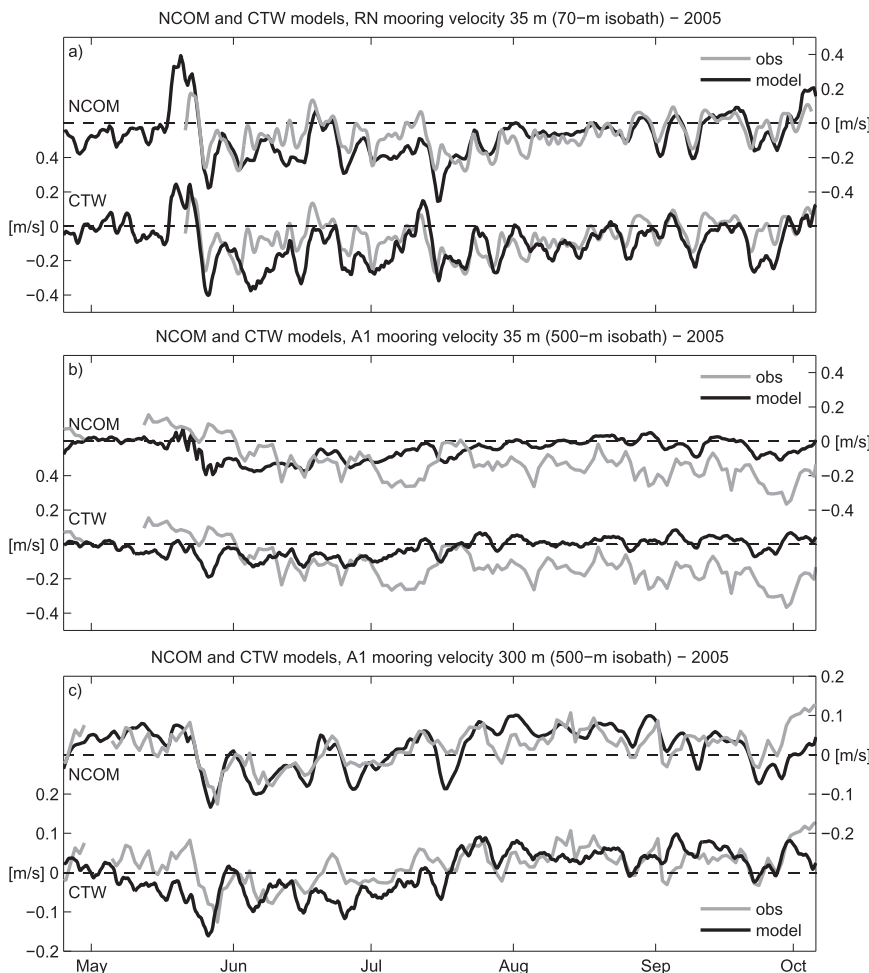


FIG. 2. Comparison of CTW and NCOM-CCS modeled alongshore velocity with current-meter measurements at (a) 35-m depth at the WA shelf RN mooring site over the 70-m isobath, (b) 35-m depth at the BC slope A1 mooring site over the 500-m isobath, and (c) 300-m depth at the BC slope A1 mooring site over the 500-m isobath. Note that a different scale has been used in (c) to show the smaller fluctuations in velocity at that location.

time series. Both models show a transition from equator- to poleward flow at this depth during summer 2005, although the CTW model tends to overestimate the magnitude of the equatorward flow. During 2004, the CTW time series indicate a similar seasonal progression as in 2005, with the strongest equatorward flow observed during April at 100 m (Fig. 4). However, at 35 m, observed equatorward velocities exceed 0.2 m s^{-1} during July, which is not reproduced in the CTW model.

Over the 500-m isobath, the largest correlations occur for both models at 100 m (Fig. 3b). All are significant at the 95% confidence level. The CC and WS statistics both indicate that NCOM-CCS outperforms the CTW model at 300 m. If comparisons are restricted to the same time period as the 2005 RN shelf measurements discussed in the previous section, the correlation with observations

improves for both models at all depths, particularly for NCOM-CCS (Fig. 3c). If time series are bandpass filtered, using a Hanning window to remove periods >20 days, correlation coefficients improve substantially for the CTW model over the slope (0.64, 0.79, and 0.60 for 35, 100, and 300 m, respectively; not shown), indicating strong agreement at weather-band time scales. The WS metric indicates that both models have relatively strong skill (~ 0.8) at 300 m and weak skill (~ 0.3) at 35 m. The weak skill at 35 m indicates that the models do not accurately represent the strength and/or cross-shore position of the equatorward shelf break jet at the A1 site. At 300 m, the modeled seasonal progression from equator- to poleward flow results in higher skill than at the surface during this time period.

A hydrographic section offshore of Copalis Beach, WA ($47^{\circ}18'N$) shows the spatial distribution of alongshore

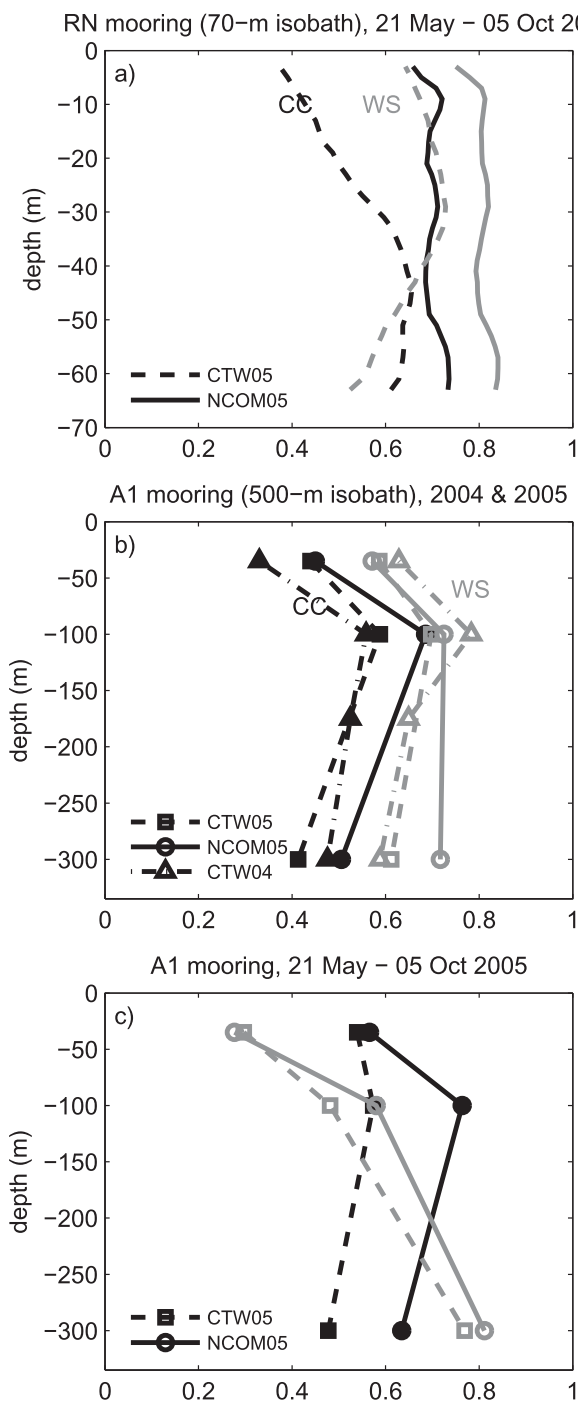


FIG. 3. Profiles of model validation statistics for (a) the RN mooring over the 70-m isobath, (b) the A1 mooring over the 500-m isobath for 2004 and 2005, and (c) the A1 mooring restricted to 21 May–5 Oct 2005 (the deployment period of the RN mooring). Black lines are CC; gray lines are WS scores.

velocity on 15 September 2005 (Fig. 5a). Over the slope, the observed core of the CUC is located at 200 m. After referencing the observations to 0.03 m s^{-1} at 500 dbar for consistency with NCOM-CCS (see section 3), the

velocity in the undercurrent core is found to be 0.09 m s^{-1} . Equatorward flow is present over the outer shelf and slope and is strongest near the surface over the 100-m isobath. Although poleward flow is present over the slope in both models (Figs. 5b,c), only NCOM-CCS shows the appropriate distribution of equatorward flow. The CTW model shows no evidence of the $\sim 0.3 \text{ m s}^{-1}$ near-surface jet that extends over the WA outer shelf and slope, unlike NCOM-CCS (Figs. 5b,c). The location of maximum equatorward flow at the surface has been observed to migrate offshore from spring to summer (Hickey 1989), a process that likely cannot be captured by the CTW model that neglects the horizontal advection of density and momentum. Weak skill at 35 m over the British Columbia slope in both models (Figs. 2b, 3c, and 4a) may be related to the complex topography of La Perouse Bank located onshore of the mooring site, as well as CTW scattering where the shelf widens from WA to BC (Wilkin and Chapman 1990; Hickey et al. 1991). The CTW model does not include scattering by alongshore variations in topography, and this process may not be accurately resolved by the 9-km resolution of NCOM-CCS.

Because the alongshore currents vary on the time scales of weather events, synoptic sections of geostrophic velocity do not necessarily represent the seasonal mean. Direct current-meter measurements across the Washington shelf and slope during the period 23 July–26 August 1972 (Hickey 1979) provide an opportunity for comparison of the model results with observations of the mean late-summer structure of alongshore velocity over the shelf and slope, although the observations are from a different year. The undercurrent is clearly present in NCOM-CCS results from the same part of the season (Fig. 5d), but the 0.09 m s^{-1} CUC core at 300–400 m is both deeper and weaker than the 0.16 m s^{-1} core at 200 m observed by Hickey (1979). During this period, the location of the undercurrent core is similar between NCOM-CCS and the CTW model (Fig. 5e), which shows a maximum poleward velocity of 0.06 m s^{-1} . The strongest mean equatorward velocity near the surface in the Hickey (1979) observations is -0.08 m s^{-1} over the outer shelf, which is much weaker than the -0.50 m s^{-1} jet during the same part of the season in NCOM-CCS. As discussed further in section 5, interannual variability is a likely reason for the difference between the 1972 observations and 2005 model results.

4. Results

Comparisons with observations in the previous section indicate that the CTW and NCOM-CCS models both capture key features of summer circulation, including

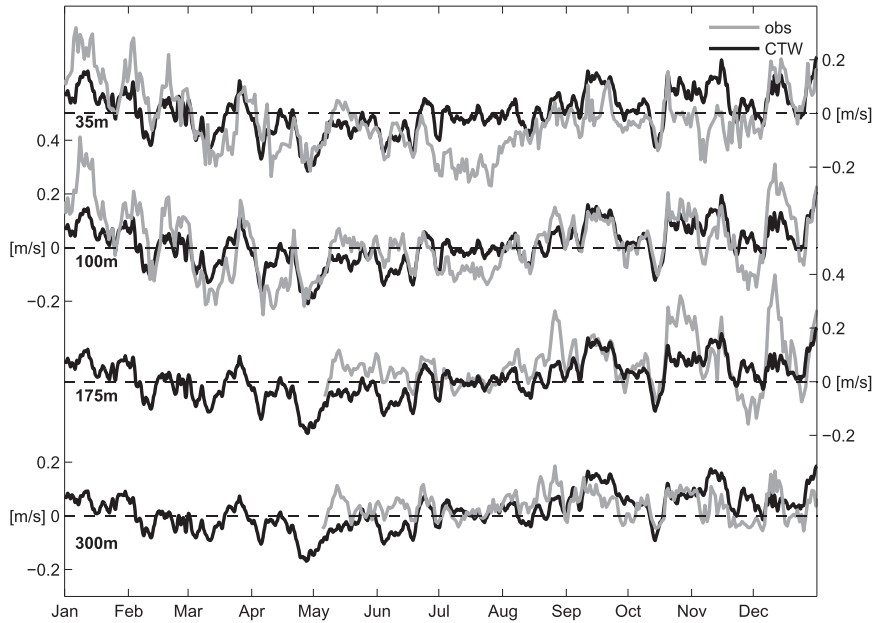


FIG. 4. Comparison of CTW modeled alongshore velocity with current-meter measurements at the A1 mooring site during 2004. Model time series are extracted from the 500-m isobath at the nominal current-meter depths 35, 100, 175, and 300 m.

equatorward flow at midshelf during summer and variability in the California Undercurrent at time scales from days to seasons. The weakest aspect of the models is the equatorward shelf break jet, which is absent from the CTW model but present over the Washington slope in NCOM-CCS (Fig. 5). To gain insight into the linear dynamics of the modeled undercurrent, the CTW model is run under different configurations to explore the sensitivity of the 2005 time series and the seasonal cycle to friction, number of modes, local wind forcing, and the southern boundary condition (section 4a). Both models are then used to determine the large-scale structure of the APF during summer (section 4b) and the balance of alongshore momentum in the northern CCS (section 4c).

a. CTW model sensitivity analysis

1) FRICTION

Previous studies, which focused on the shelf, have shown that the value of the linear frictional coefficient can influence the amplitude and phase of modeled velocity fluctuations (Battisti and Hickey 1984; Chapman 1987). To examine how friction modifies the response over the shelf and slope, the original value of $r = 2.5 \times 10^{-4} \text{ m s}^{-1}$ was reduced to $r = 1.0 \times 10^{-4} \text{ m s}^{-1}$, and also increased by the same amount to $r = 4.0 \times 10^{-4} \text{ m s}^{-1}$. The weaker frictional coefficient enhances the modeled equatorward velocity over the midshelf, which reaches -0.6 m s^{-1} during early June (Fig. 6a, top), much larger

than the observed peak velocity of -0.3 m s^{-1} (Fig. 2a). An equivalent increase in r has a smaller effect on the strength of equatorward flow over the midshelf (Fig. 6a, top). At 300 m over the slope, decreasing r enhances poleward flow and increasing r reduces the magnitude of poleward flow during late summer (Fig. 6b, top), with resulting differences $< 0.05 \text{ m s}^{-1}$.

2) NUMBER OF MODES

The number of modes used varies substantially among studies (Clarke and Van Gorder 1986). In this study, convergence was found for three modes and more. During mid-July–October 2005, the use of two or more modes enhances equatorward flow over the shelf (Fig. 6a, upper middle) and enhances poleward flow at 300 m over the slope (Fig. 6b, upper middle). During June and early July, the first mode dominates the response. Higher modes tend to be locally generated because they have greater values of a_{mn} and are preferentially damped as they travel away from the forcing region. Therefore the higher modes tend to be more important after the onset of strong local wind stress in mid-July.

3) LOCAL WIND STRESS

During summer, remote wind stress contributes to weather-band variability over the Washington shelf (Battisti and Hickey 1984). To explore the role of remote forcing over the slope, the CTW model was run with local wind forcing $\tau^y = 0$ at locations north of 42°N .

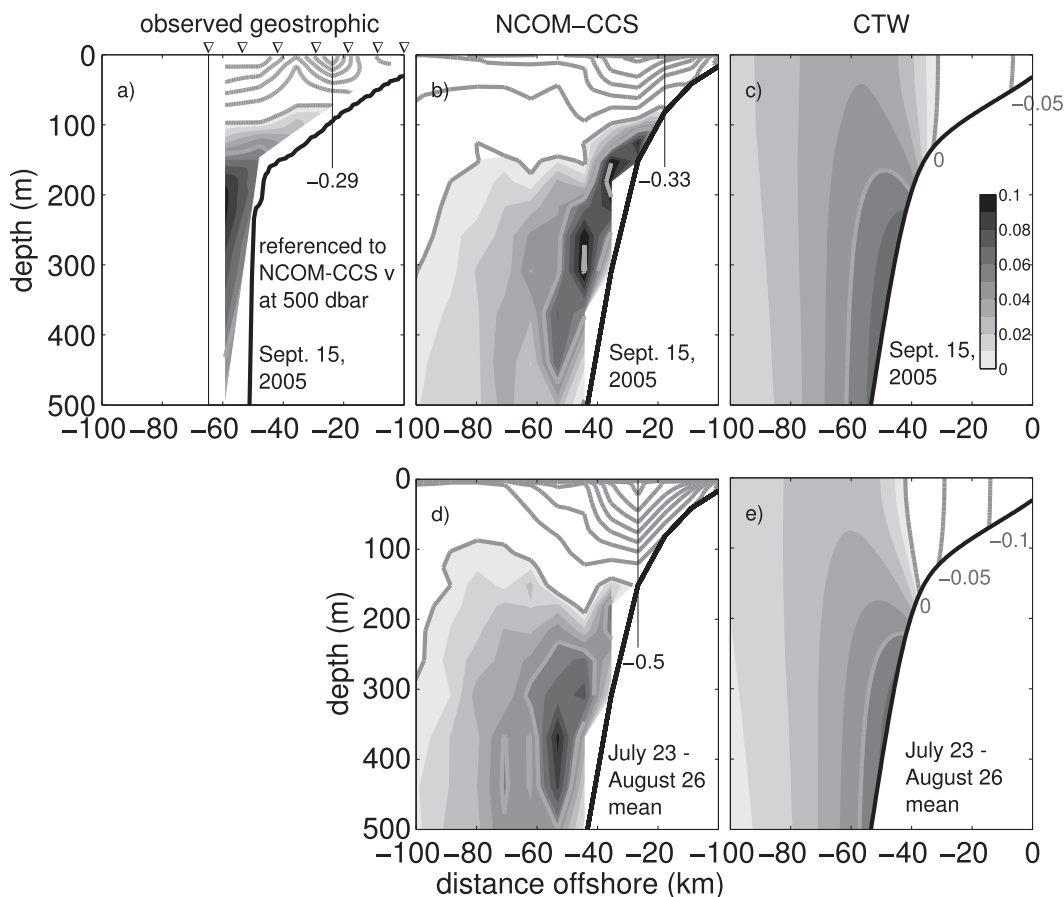


FIG. 5. Sections of alongshore velocity off the WA shelf. (a) Observed geostrophic velocity on 15 Sep 2005, referenced to 0.03 m s^{-1} at 500 dbar for consistency with NCOM-CCS results. Triangles indicate locations of CTD casts. (b) NCOM-CCS results for 15 Sep 2005. (c) CTW model results for 15 Sep 2005. (d) Time average of NCOM-CCS results for 23 Jul–26 Aug 2005. (e) Time average of CTW model results for 23 Jul–26 Aug 2005. Contour intervals are 0.05 m s^{-1} , and poleward flow is shown in shades of gray with 0.01 m s^{-1} intervals. Labels indicate the location and magnitude of the strongest equatorward velocity.

This configuration retains the relatively strong wind forcing off northern California and removes the relatively weak forcing north of Cape Blanco, Oregon (Fig. 1c). During 2005, the local wind stress transitioned to equatorward over one month later than usual in late May and remained anomalously weak through mid-July (Hickey et al. 2006; Kosro et al. 2006). Over the shelf (Fig. 6a, lower middle), remote forcing is responsible for the strong equatorward flow ($v \sim 0.4 \text{ m s}^{-1}$) during this early period of weak winds. The remotely driven shelf velocity later in the summer during August is weaker, with more frequent poleward flow events. In contrast to the shelf, removing the local wind stress has little effect on the flow over the slope at 300 m, aside from introducing a lag of several days (Fig. 6b, lower middle). The difference between the shelf and slope can be understood by considering the role of the various modes

described in the previous section. Removal of local equatorward wind stress weakens the equatorward flow associated with the first mode over both the shelf and slope. However, the suppression of locally generated higher modes results in weaker equatorward flow over the shelf and weaker poleward flow over the slope. These two effects counteract each other over the slope but reinforce each other over the midshelf, resulting in greater sensitivity to local wind stress over the midshelf.

4) SOUTHERN BOUNDARY CONDITION

The CTW model includes signals created at the southern boundary of the model in addition to those generated by wind forcing farther north along the west coast of North America. The southern boundary condition relies on the assumption that fluctuations in

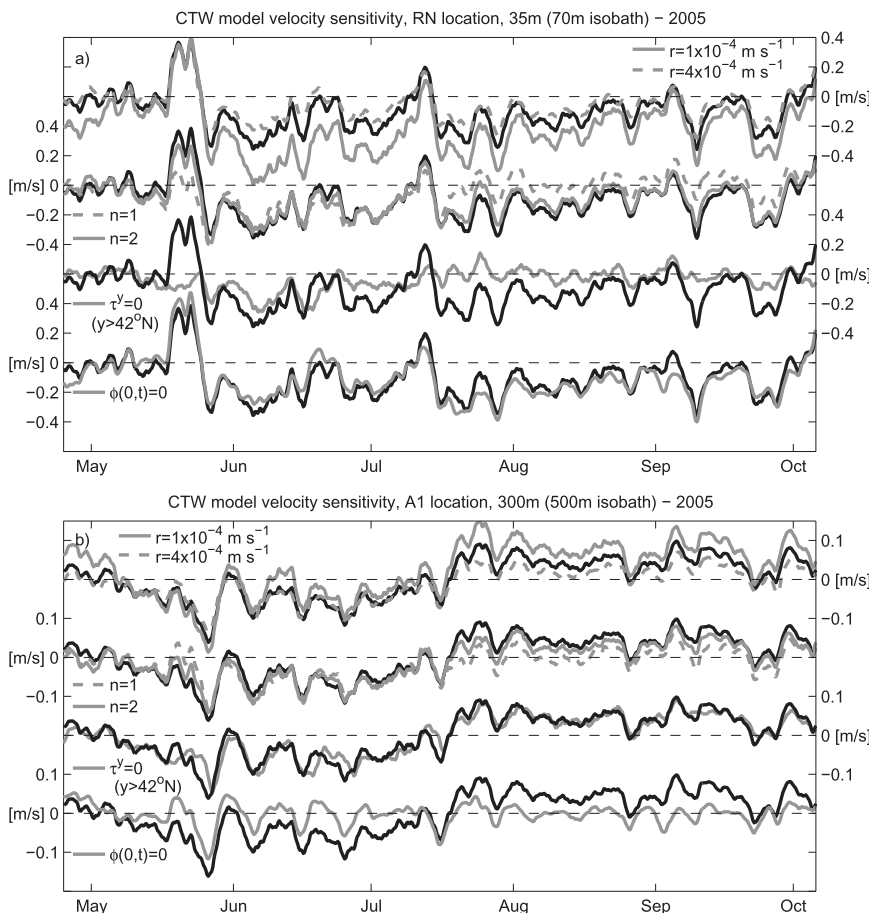


FIG. 6. Time series of alongshore velocity showing sensitivity to parameters used in the CTW model at (a) 35 m over the 70-m isobath at the RN site over the WA shelf and (b) 300 m over the 500-m isobath at the A1 site over the BC slope. In each row, the solid black is the base run. Additional runs with the frictional coefficients $r = 1 \times 10^{-4} \text{ m s}^{-1}$ (solid gray) and $r = 4 \times 10^{-4} \text{ m s}^{-1}$ (dashed gray) (top), 1 (dashed gray) and 2 modes (solid gray) (upper middle), no wind forcing north of 42°N (solid gray) (lower middle), and no energy at the southern boundary (solid gray) (bottom) are shown.

adjusted sea level at San Diego are associated with first-mode coastal trapped waves. To show the effect of this southern boundary condition on the model results, we use an alternative boundary condition of $\phi_1(0, t) = 0$, representing zero wave energy at the southern boundary.

Over the midshelf, the southern boundary condition (Fig. 6a, bottom) does not have as much of an effect on the modeled velocity as the elimination of the local wind stress (Fig. 6a, lower middle). However, the southern boundary does have a significant effect on the modeled velocity over the slope (Figs. 6b, bottom). Without using the San Diego sea level at the southern boundary, the 300-m velocity time series lacks the observed persistence of equatorward flow during spring and poleward flow during late summer and early fall. Poleward flow events

still occur and are much more frequent than over the shelf, but equatorward flow events are also common during late summer.

Seasonal-mean sections further demonstrate the influence of sea level variability on alongshore velocity in the northern CCS (Fig. 7). In the NCOM-CCS (Fig. 7, top) and the CTW model with San Diego sea level variability included (Fig. 7, middle), poleward flow is a maximum of $\sim 0.05 \text{ m s}^{-1}$ at 300–400 m during summer, intensifies near the coast during the fall and winter, and disappears during spring when equatorward flow dominates. Although the offshore extension and vertical shear of equatorward flow are more realistic in NCOM-CCS during summer (section 3; Fig. 5), the development of equatorward flow over the shelf and slope during spring and the intensification of poleward flow over the

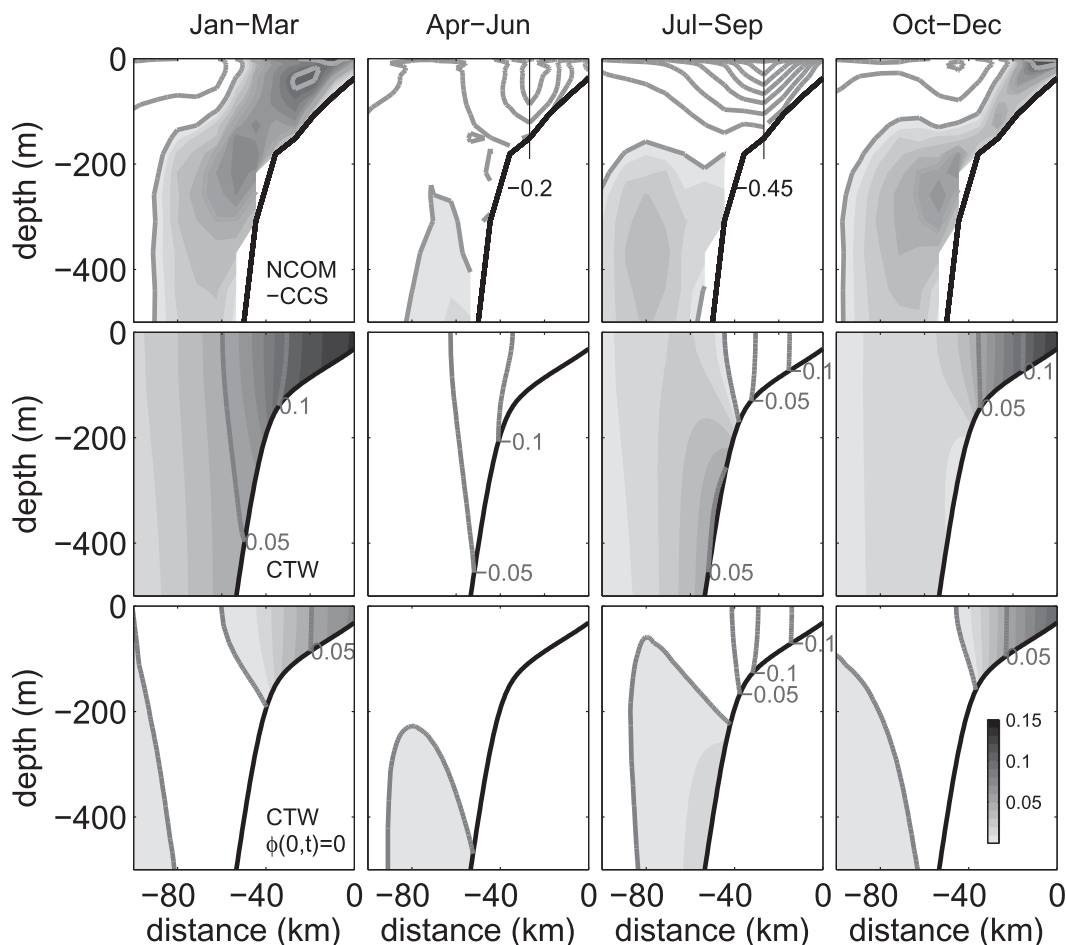


FIG. 7. Seasonal means of modeled alongshore velocity at 47°N during (far left) January–March 2005, (middle left) April–June 2005, (middle right) July–September 2005, and (far right) October–December 2005. Results are shown for the (top) NCOM-CCS, (middle) CTW model, and (bottom) CTW model with no wave energy at the southern boundary. Contour intervals are 0.05 m s^{-1} , and poleward flow is shown in shades of gray with 0.01 m s^{-1} intervals.

slope during summer in both models are consistent with observational studies in the northern CCS (Hickey 1979; Collins et al. 2003; Thomson and Krassovski 2010).

In the case with no CTW energy at the southern boundary (Fig. 7, bottom), the modeled undercurrent is weaker in the summer mean ($\sim 0.02 \text{ m s}^{-1}$) (Fig. 7). In addition, poleward flow over the shelf during fall and winter as well as equatorward flow during the spring are substantially weakened in comparison to the case that includes San Diego sea level variability. Additional runs that include winds off Baja California, south of San Diego, showed no improvement in the modeled seasonal variations in the northern CCS (not shown). Although CTW dynamics associated with wind forcing alone can generate weak mean poleward flow over the northern CCS slope during summer (Fig. 7), and increase poleward

flow at the time scale of weather events (Fig. 6b), the magnitude and timing of its seasonal cycle more closely resemble observations and NCOM-CCS with the use of San Diego sea level at the southern boundary.

b. Large-scale structure of the APF during summer

The structure of the poleward APF, which opposes the prevailing equatorward wind stress during summer, is important for understanding dynamics associated with the CUC. Although the sea level gradient determines the APF near the surface, the APF may be substantially modified at depth by the presence of alongshore density gradients. Cross-shelf structure may also be present due to the shelf topography and coastal trapping. In this section, we use the NCOM-CCS and CTW models to gain insight into the structure and variability of the APF. Seasonal differences in the APF during 2005 are first

examined near the coast, where tide gauge observations are available. Analysis of the modeled APF is then extended offshore to the continental slope, where the models provide a more complete view of its timing and spatial structure.

1) VARIABILITY IN COASTAL SEA LEVEL

Winter-to-summer differences in sea level are compared at different locations along the coast during January–March and 15 June–15 September 2005 (Fig. 8a). The latter period is chosen because flow transitions seasonally from equator- to poleward at 300 m over the slope (Fig. 2c). Differences between the 3-month averages are examined first, because the tide gauge observations cannot be used to estimate the absolute spatial gradients during each individual season. Between these two periods, referred to as “winter” and “summer” conditions, the observed sea level drops to lower values along the entire coastline from Point Conception to Vancouver Island (Fig. 8a), consistent with the development of equatorward geostrophic currents near the coast.

Modeled winter-to-summer differences in sea level follow latitudinal patterns similar to those of the observations, showing larger seasonal decreases in the northern CCS (Fig. 8a). Both models underestimate the overall magnitude of the sea level decrease at all latitudes. Relative differences along the coast in NCOM-CCS parallel those in the observations, and the CTW model shows a weaker alongshore gradient in the seasonal differences. To reproduce the magnitude of the observed sea level gradient in a steady barotropic model, Hickey and Pola (1983) used a smaller frictional coefficient of $r = 1 \times 10^{-4} \text{ m s}^{-1}$. Using this value in the CTW model results in a larger alongshore gradient (Fig. 8a), but also produces unrealistically strong equatorward flow over the WA shelf (up to 0.6 m s^{-1} ; Fig. 6, top).

Absolute gradients in coastal sea level from the numerical models can be compared with observations if the tide gauge data are added to the mean dynamic height estimated from the climatology. Following Hickey and Pola (1983), mean dynamic height data at the coast from Reid and Mantyla (1976), referenced to 500 dbar, are interpolated to the tide gauge locations. During winter 2005, the NCOM-CCS and CTW models both show higher average sea level in the northern CCS, consistent with the observations (Fig. 8b). During summer, coastal sea level in NCOM-CCS slopes $\sim 0.10 \text{ m}$ downward from PSL in the south to NH farther north, consistent with the observed alongshore gradient. Farther north from NH to LP, the observed sea level gradient indicates

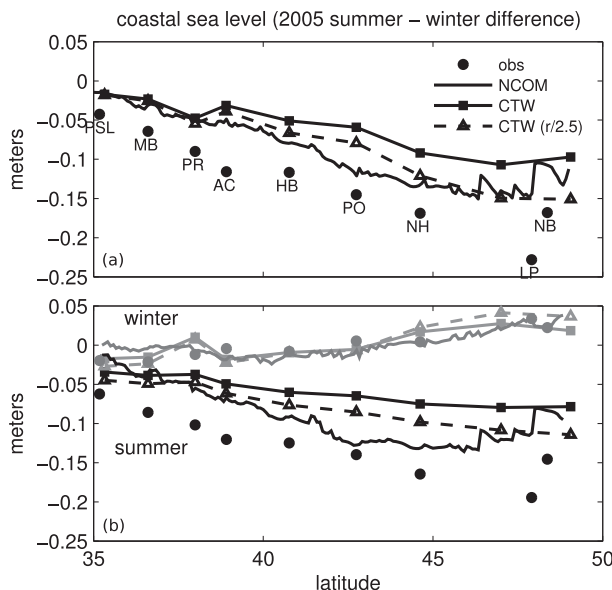


FIG. 8. Winter-to-summer differences in coastal sea level from Point Conception to Vancouver Island during 2005. (a) Difference of seasonal averages from adjusted tide gauge observations (gray) and NCOM-CCS (black line), CTW (squares) and CTW with the drag coefficient reduced by a factor of 2.5 (triangles). Winter is defined as January–March; summer is defined as 15 Jun–15 Sep. (b) Summer and winter averages of sea level for the three models and observations, referenced to the latitude-averaged mean winter value. Observations are estimated by adding tide gauge data to the mean dynamic height climatology of Reid and Mantyla (1976).

a poleward APF at the coast; additional data in northern CCS indicate that this pattern is robust (R. McCabe and B. M. Hickey 2013, unpublished manuscript). In contrast, the sea level gradient in NCOM-CCS indicates a weak equatorward APF at the coast from northern OR to southern BC. Smaller-scale variability occurs between LP and NB in NCOM-CCS and observations. In the CTW model, coastal sea level in the northern CCS slopes either very weakly up- or downward to the north, depending on which drag coefficient is used. Although the absolute gradient in the coastal sea level varies between models in the northern CCS, all models reproduce the seasonal development of the CUC (section 3). As will be shown in the following section, this is due to the importance of the baroclinic component of the APF over the slope.

Modeled intraseasonal variability in the APF over the shelf can be assessed by comparing with observed variability in alongshore gradients of coastal sea level. Intraseasonal fluctuations in the observed surface APF ($-g\eta_x$, where η is sea surface height at the coast) between NH and NB during 2005 are more correlated with remote alongshore wind stress near HB, over 400 km south of Newport, than with local wind stress (Fig. 9).

The APF is directed most poleward following wind relaxations or reversals to the south, and the lags of the maximum correlation with wind stress along the coast suggest a response that travels at approximately twice the free-wave CTW phase speed. This propagation speed of the pressure response is consistent with analytical solutions to (7) forced by periodic wind stress with the alongshore structure (Philander and Yoon 1982). Modeled alongshore gradients in coastal sea level are significantly correlated with observations in the CTW model ($CC = 0.52$; Fig. 10a) and more strongly correlated with observations in NCOM-CCS ($CC = 0.87$; Fig. 10b). Correlation between the observed and modeled APF at the coast indicate that the models can be used to understand the variability of the APF farther offshore over the slope.

2) THE APF AT UNDERCURRENT DEPTHS

Analysis of the modeled APF is now extended from the coast to the slope, where the CUC is located. To evaluate the slope APF at the same alongshore scale as the coastal sea level gradients, two end points from the same latitudes as NB and NH are selected. Perturbation pressure is defined as

$$p'(x, y, z, t) = p(x, y, z, t) - \bar{p}(z), \quad (9)$$

where $\bar{p}(z)$ is a reference pressure calculated from a mean density profile, which does not contribute to horizontal gradients.

Shelf-to-slope differences in the modeled APF are significant during summer (Fig. 10c). Compared with the surface APF at the coast, fluctuations have a smaller magnitude near the bottom at 309 m over the slope, and there is no significant correlation between the APF at the two locations. This lack of correlation is likely due to higher-mode waves. The spatial and temporal variability of bottom pressure at 309 m during this period shows several poleward-propagating signals with phase speeds that vary between events (Fig. 10d). An example during late May 2005 is highlighted in which a low pressure signal propagates northward at approximately twice the phase speed of a free first-mode CTW, followed by a high pressure signal at approximately twice the phase speed of a free second-mode CTW. During this event, a poleward APF develops over the slope during the transition from low to high pressure and is enhanced by the poleward decay of the high pressure signal (Figs. 10c,d). Similar patterns can be found, for example, in the time periods leading up to the next poleward APF event during early June and the strongest poleward APF event during mid-July.

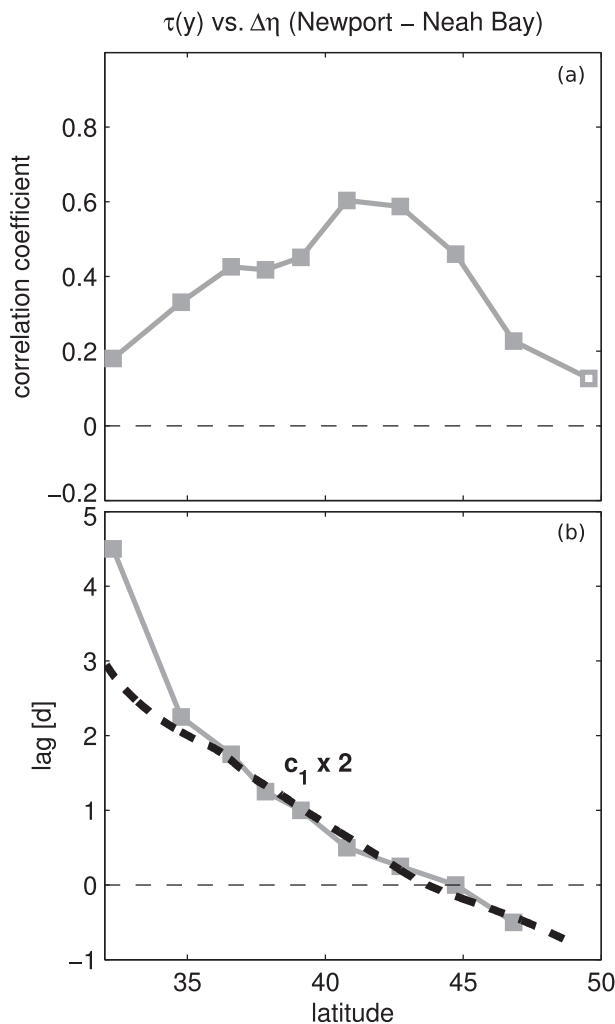


FIG. 9. (a) Correlation coefficient between observed sea level difference (NH - NB) and CCMP wind stress at various latitudes. Filled squares indicate significance at the 95% confidence level. (b) Lag (days) of max correlation.

The summer means of modeled perturbation pressure and SSH are used to further examine the large-scale spatial structure of the APF with depth and latitude over the slope (Fig. 11). South of 42°N, the mean SSH over the slope during 15 June–15 September is consistent with a large-scale poleward APF at the surface (Fig. 11a). North of 42°N over the slope, higher SSH to the north indicates a mean equatorward APF at the surface. These large-scale patterns in the surface APF are consistent at multiple isobaths over the slope. Smaller-scale variability ($<1^\circ$ latitude) is also present in the northern CCS. Distributions of mean bottom pressure over the slope (Fig. 11b) reveal a large-scale poleward APF at all latitudes from Point Conception to Vancouver Island. The large-scale APF at the bottom is weaker at isobaths

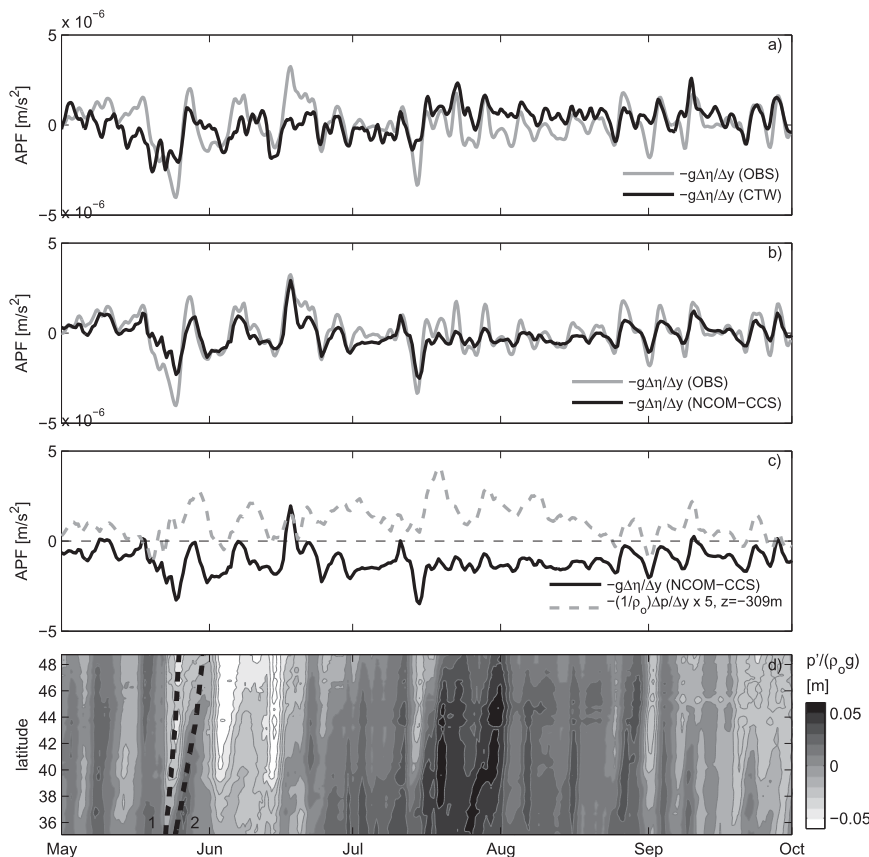


FIG. 10. Time series of observed and modeled alongshore pressure gradients during May–September 2005. (a) Observed NH – NB sea level gradient (gray) and CTW sea level gradient from WA coast segment (black). (b) Observed NH – NB sea level gradient (gray) and sea level gradient calculated from the same coastal locations in NCOM-CCS (black). (c) Sea level gradient calculated from the same coastal locations in NCOM-CCS, with bottom pressure gradient at 309 m calculated from points at the same latitudes (dashed gray). The bottom pressure gradient at 300 m is multiplied by a factor of 5 for clarity. (d) Bottom perturbation pressure at $z = -309$ m, from Point Conception to Vancouver Island. Dashed lines indicate the anticipated propagation of forced first- and second-mode CTWs (twice the free-wave phase speeds).

deeper and farther offshore. The horizontal distribution of perturbation pressure in the water column over the 309-m isobath (Fig. 11c) shows that depths >150 m are characterized by lower pressure to the north at all latitudes, indicative of a poleward APF throughout the CCS at depths below the shelf break.

The pressure distribution over the slope indicates that the summer-mean poleward APF at undercurrent depths in the northern CCS is associated with alongshore density gradients, not a sea surface that slopes downward to the north. Over the upper slope, maximum upward displacement of the $\sigma_t = 26.5$ isopycnal occurs at 42°N (Fig. 11d). The $\sigma_t = 25.5$ isopycnal slopes downward to the north at 42°N and lighter isopycnals (e.g., $\sigma_t = 24.5$) also slope downward to the north in the northern CCS. Therefore, at the latitude of minimum sea level over the slope and latitudes farther north,

alongshore density gradients are responsible for the poleward APF at undercurrent depths. Farther south, the alongshore density gradients weaken the stronger poleward APF at the surface. Similar to NCOM-CCS, the maximum density anomaly in the CTW model occurs near 42°N (Fig. 11e). While the magnitude of these anomalies are about an order of magnitude greater in NCOM-CCS, the pattern of upward isopycnal displacement centered at 42°N is consistent with CTW dynamics. This upward displacement, most pronounced in the $\sigma_t = 26.5$ isopycnal, does not appear to result from offshore forcing because it is much weaker over the 1055-m isobath in NCOM-CCS (Fig. 11f).

The CTW model can be used to evaluate contributions to the APF from alongshore wind forcing along the U.S. West Coast and remote signals farther south. The cross-shore structure of the large-scale APF is clearly

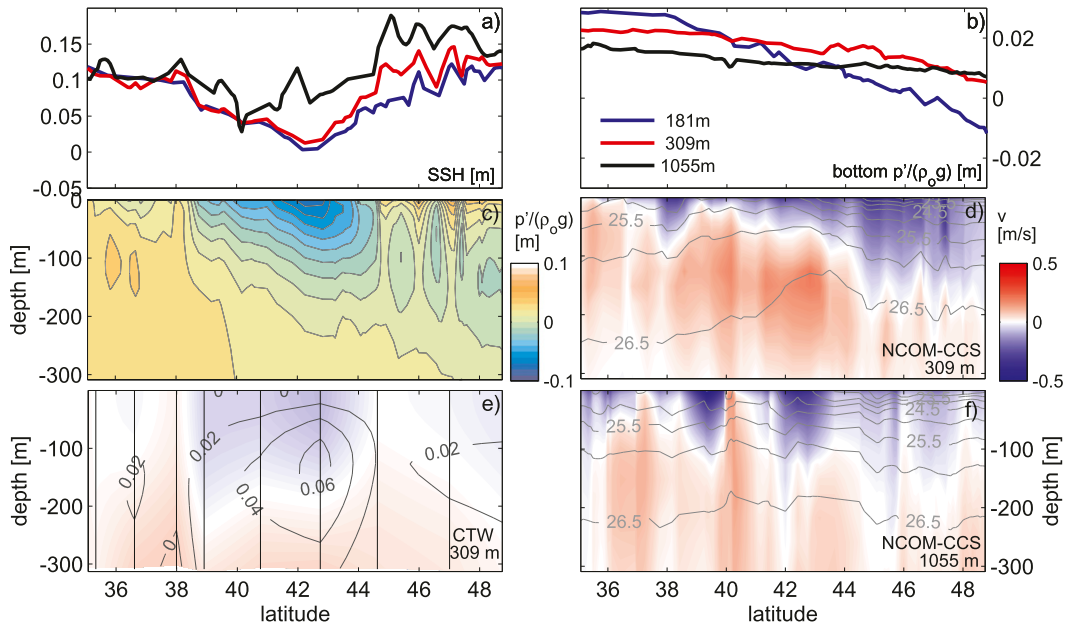


FIG. 11. Modeled mean alongshore structure over the slope during 15 Jun–15 Sep 2005. (a) NCOM-CCS SSH over three isobaths, (b) NCOM-CCS bottom perturbation pressure over three isobaths, normalized to units of dynamic height. (c) NCOM-CCS perturbation pressure over the 309-m isobath. (d) NCOM-CCS velocity v and σ_t (contours) over the 309-m isobath. (e) CTW alongshore v (colors) and density anomaly (contours) over the 309-m isobath. (f) NCOM-CCS velocity v and σ_t (contours) over the 1055-m isobath. Note the smaller contour interval for CTW density anomaly compared with NCOM-CCS σ_t .

defined in the CTW model, because the bathymetry is uniform in the alongshore direction within each segment. During 15 June–15 September 2005, the poleward APF in the northernmost segment of the CTW model is strongest near the bottom at the shelf break, and an equatorward APF is present over the shelf near the coast (Fig. 12a). Farther south in the CTW model, at the 47°N Washington segment, the strongest poleward APF occurs closer to shore over the shelf (Fig. 12d). At the 40.8°N HB segment, closer to the strongest wind forcing, the poleward APF is strongest at the surface and near the coast (Fig. 12g).

The stronger poleward APF at the depth over the slope (Fig. 12a) again demonstrates the importance of alongshore density gradients at locations north of the strongest wind stress in the CCS. Unlike the NCOM-CCS summer mean (Fig. 11a), the CTW model does not have an equatorward surface APF over the northern CCS slope, which may be associated with the equatorward shelf break jet that is absent from the CTW model. However, the NCOM-CCS and CTW models both indicate enhancement of the poleward APF at depth over the slope by alongshore density gradients. In the following section, it will be shown that the modeled poleward APF over the northern CCS slope is largely

balanced by a Coriolis force associated with onshore flow at time scales from weeks to months.

c. Alongshore momentum balance over the northern CCS slope

In a linear model, the alongshore momentum balance away from the frictional boundary layers is described by

$$v_t + fu = -\rho_0^{-1}p_y. \quad (10)$$

The CTW model indicates that during summer the mean APF $-\rho_0^{-1}p_y$ is primarily balanced by the mean Coriolis force fu (Figs. 12b,e,h), which is much greater than the mean acceleration v_t (Figs. 12c,f,i). In this section, temporal variability in (10) is examined. The validity of a linear alongshore momentum balance is assessed, and it is shown that the dominant terms in the alongshore momentum balance are dependent on the time scale of interest, with the Coriolis force largely balancing the APF at >20-day time scales.

The validity of the linear momentum balance over the slope can be examined using the nonlinear NCOM-CCS. To remove mesoscale variability and focus on the alongshore scale of the northern CCS slope, NCOM-CCS time series have been averaged over 44.5°–48.5°N

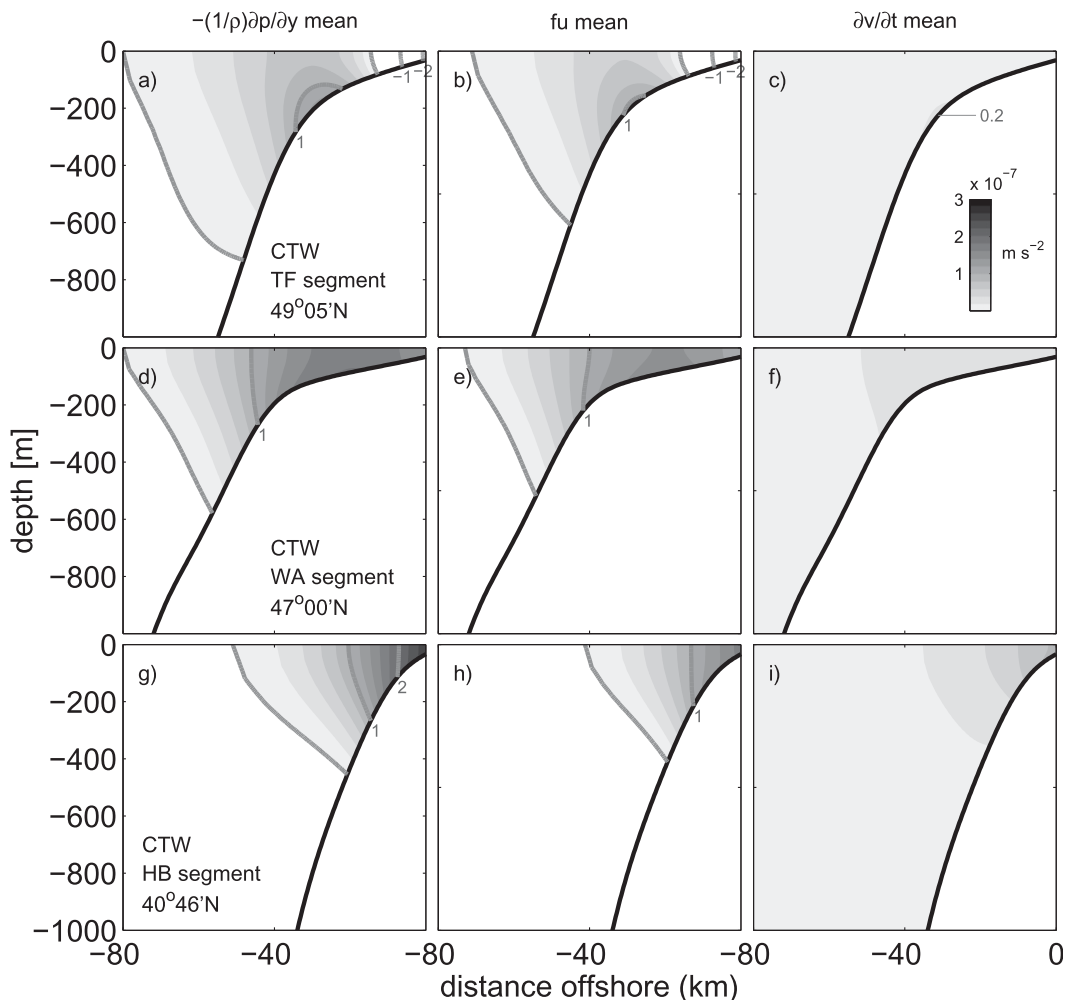


FIG. 12. Seasonally averaged momentum balance terms from the CTW model during 15 Jun–15 Sep 2005: (a) mean APF, (b) mean Coriolis force, and (c) mean acceleration at the TF segment off the British Columbia coast (see Fig. 1). (d)–(f) As in (a)–(c), but for the WA segment (see Fig. 1). (g)–(i) As in (a)–(c), but for the HB segment off the northern coast of California. Contour intervals are $1 \times 10^{-7} \text{ m s}^{-2}$, with positive values shaded at $0.2 \times 10^{-7} \text{ m s}^{-2}$ intervals.

and 3 grid points offshore of the 309-m isobath. To separate variability at time scales of several weeks or longer from weather-band variability, low-frequency time series have been created by filtering with a 20-day Hanning window.

In the low-frequency, spatially averaged NCOM-CCS time series, the undercurrent accelerates and shoals during summer (Fig. 13a). The APF and Coriolis force resemble each other closely in timing, magnitude, and depth structure (Figs. 13b,c). Although there is a mean baroclinic depth structure (Fig. 11c), a surface-intensified poleward APF is present during July (Fig. 13b). Acceleration is generally an order of magnitude smaller than the APF and Coriolis force at these longer time scales (Fig. 13d). Agreement between acceleration

and the residual of the Coriolis force and APF away from the surface boundary layer indicates that the linear balance is valid over the slope, especially at 100–300 m (Figs. 13d,e).

At a typical undercurrent depth, 50 m above the bottom boundary layer at 259 m, the dominant terms of the momentum balance depend on the time scale analyzed. At shorter time scales (<20-day periods), the APF is generally smaller than the acceleration and Coriolis force terms (Fig. 14). The timing and magnitude of the momentum balance terms are consistent between the NCOM-CCS and CTW models. Correlations between models are 0.55, 0.50, and 0.49 for the acceleration, Coriolis, and APF terms, respectively, with a 1-day lag in the APF term.

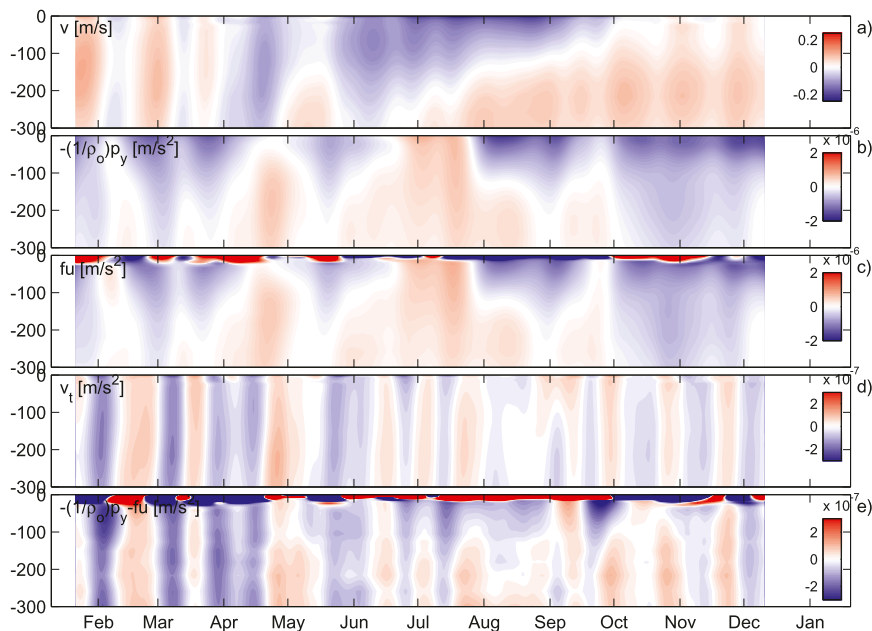


FIG. 13. Velocity and linear momentum balance terms (20-day period and greater) over the northern CCS slope (44.5° – 48.5° N) during 2005 from NCOM-CCS: (a) alongshore velocity, (b) APF, (c) Coriolis force, (d) alongshore acceleration, and (e) residual of the APF and Coriolis force. Note the color scale difference between (b)–(c) ($\times 10^{-6}$) and (d)–(e) ($\times 10^{-7}$).

At longer time scales, the Coriolis force largely balances the APF and leads the APF by 2 days in NCOM-CCS (Fig. 15a). In the CTW model, the Coriolis force and APF are weaker and not as strongly correlated (Fig. 15b). However, the seasonal timing of the APF is similar in the two models, with maxima in the poleward APF during late April and mid-July. In both models, the poleward APF is persistent during the period June–August. The acceleration term (not shown) is weak and lacks a persistent summer mean (see Figs. 12, 13). With wind forcing only [$\phi_1(0, t) = 0$], the Coriolis term and the APF are weaker, but onshore flow and the poleward APF are still persistent during summer (Fig. 15c). Even though the mean poleward velocity during summer is weaker in the wind-only case (Figs. 6b, 7), the seasonal development of the poleward APF over the northern CCS slope is a robust part of each model run and therefore is largely associated with wind forcing along the U.S. West Coast.

5. Summary and discussion

This study uses two numerical models with different levels of complexity to examine the dynamics of the poleward CUC and APF. Time series observations of alongshore velocity over the continental slope allow for a detailed assessment of modeled variability over time scales from days to seasons. Processes influencing the

CUC and APF are illustrated schematically in Fig. 16, and major results are summarized below:

- Seasonal development of a persistent CUC during late summer in the northern CCS is primarily dependent on incoming energy from sea level variability applied south of the region of strong coastal wind forcing, while event-scale fluctuations over the northern CCS slope at CUC depths are primarily forced by remote coastal wind events (section 4a).
- The APF over the continental slope has barotropic and baroclinic components. At time scales from weeks to months in the northern CCS, the baroclinic APF provides a poleward force at CUC depths, which is balanced by the Coriolis force associated with onshore flow. In the central and southern parts of the CCS, the baroclinic component weakens the barotropic APF at CUC depths (sections 4b–c).

An unanticipated result of this study is the dependence of a persistent late-summer CUC on the use of the San Diego sea level at the southern boundary. Low adjusted sea level at San Diego during spring is associated with strong equatorward flow, while high adjusted sea level is associated with a poleward-flowing inshore countercurrent (Reid and Mantyla 1976). This near-surface poleward flow is evident in the mean NCOM-CCS sea surface height field during summer

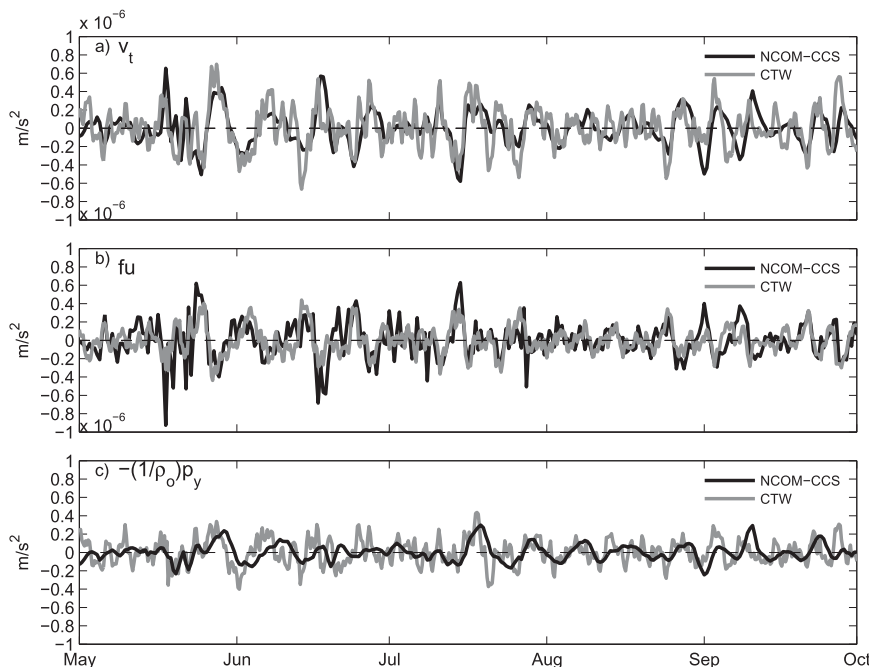


FIG. 14. Modeled linear momentum balance terms (<20-day periods only) during 2005 from the NCOM-CCS and CTW models: (a) acceleration, (b) Coriolis force, and (c) APF. Time series are for 50 m from the bottom over the 309-m isobath. NCOM-CCS time series are averaged over 44.5°–48.5°N, and CTW time series are from the WA coast segment.

(Fig. 1a). Model results have shown that remote forcing from the equatorial Pacific contributes to the annual cycle of sea level in the CCS (Pares-Sierra and O’Brien 1989). More recently, Shulman et al. (2010) linked observations of anomalously high coastal sea level during summer 2006 to propagating signals originating near the equator in the global NCOM model. The importance of the southern boundary at seasonal time scales suggests a possible dynamic link between poleward flows often considered to be separate: the undercurrent as far north as British Columbia and the inshore countercurrent in the southern CCS.

This result contrasts with the study of Chapman (1987), who found that including San Diego sea level as a southern boundary condition weakened the correlation with observed bottom pressure over the northern CA shelf. In the present study, the southern boundary of the CTW model primarily influences the northern CCS at a time scale of months, which Chapman (1987) did not analyze. It is possible that smaller-amplitude weather-band fluctuations at San Diego are generated more locally than the lower-frequency fluctuations and are therefore associated more with higher-mode CTWs that do not propagate far north. It is also possible that the shorter-period weather-band fluctuations are more susceptible to scattering by alongshore variations in

topography, which most likely occurs where the coastline bends sharply near Point Conception (south of PSL; Fig. 1a). Johnson (1991) shows that scattering can be limited either if stratification is strong or if frequencies are much less than N/α , where α is the bottom slope. For characteristic values near Point Conception, $N^2 = 10^{-4} \text{ s}^{-2}$ and $\alpha = 5 \times 10^{-3}$: this corresponds to a period of ~ 1.5 days, which is comparable to the time scales in the weather band.

Outside of the northern CCS, undercurrent dynamics may be more strongly influenced by processes such as wind stress curl that are not present in the CTW model dynamics or implicitly included in the southern boundary condition. McCreary et al. (1987) and Batteen (1997) found that wind stress curl creates a stronger and shallower poleward undercurrent. However, remote wind stress curl is not thought to influence coastal currents in the same way as remote alongshore wind stress (McCreary et al. 1987). Poleward flow induced by the alongshore gradient of wind stress curl weakening to the south may influence remote locations (Oey 1999), but it is unclear how this mechanism would generate poleward flow in the northern CCS. Wind stress curl is relatively weak in the northern CCS and strongest off northern California and in the Southern California Bight (Bakun and Nelson 1991).

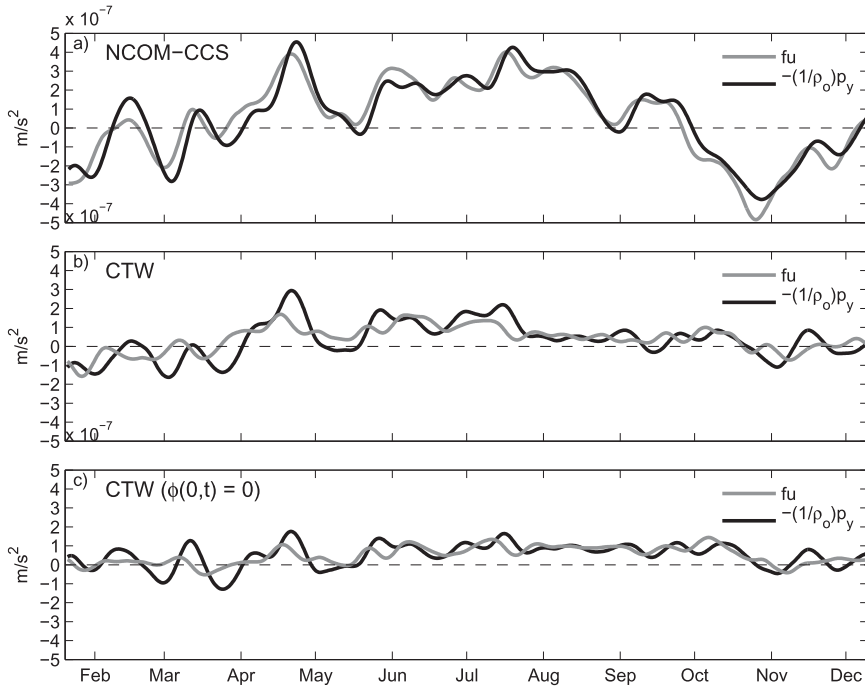


FIG. 15. Modeled APF and Coriolis force terms (20-day period and greater) over the northern CCS slope during 2005. (a) NCOM-CCS, (b) CTW model, and (c) CTW model run with no wave energy at the southern boundary. All time series are from 259-m depth over the 309-m isobath, as in Fig. 14. NCOM-CCS time series are averaged over 44.5°–48.5°N, and CTW time series are from the WA coast segment.

Another factor missing from the CTW model is the β effect, which in idealized studies has been found to strengthen the poleward undercurrent and APF at seasonal time scales (Philander and Yoon 1982; Suginohara

and Kitamura 1984). Observations in the southern CCS have revealed offshore propagation of poleward flow structures consistent with baroclinic Rossby waves (Todd et al. 2011). However, it remains unclear how

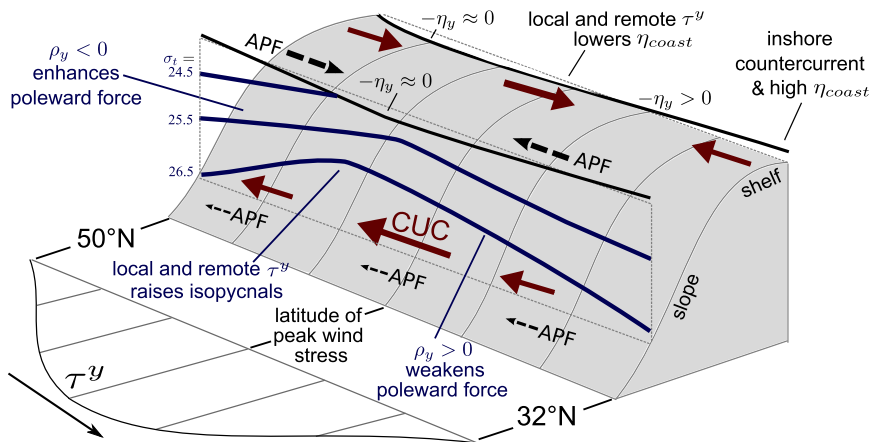


FIG. 16. Schematic of processes influencing the CUC and APF during summer. The term $-\eta_y$ represents the alongshore pressure gradient force associated with sea level η_{coast} represents sea level at the coast, ρ_y represents the alongshore density gradient over the slope, and τ_y represents the alongshore component of wind stress. Solid red arrows represent currents, black dashed arrows represent the APF, and thick blue lines represent isopycnals intersecting a vertical plane over the slope.

important the β effect is at seasonal and shorter time scales farther north of Washington and British Columbia. At the annual time scale, Rossby wave propagation only occurs south of a critical latitude, estimated to be $\sim 42^\circ\text{N}$ in the CCS (Clarke and Shi 1991).

Topographic rectification is another process that is absent from the CTW model but could be present in NCOM-CCS. In the presence of stratification, the rectification of oscillating flow over topography that varies in the along-shelf direction produces a mean poleward flow concentrated over the upper slope. The modeling study of Brink (2011) shows that parameters representative of the northern CCS result in a $\sim 0.1\text{ m s}^{-1}$ mean poleward flow. In addition, topographic rectification can also lead to a large-scale gradient in coastal sea level that slopes downward in the direction of wave propagation (Brink 2010). It is therefore possible that topographic rectification could explain the stronger poleward flow and coastal sea level gradient in NCOM-CCS compared with the CTW model during summer, although the $\sim 40\text{ km}$ topographic length scale is only coarsely resolved by the 9-km-resolution NCOM-CCS. Because the topographic rectification theory provides scaling for the mean flow, it is not immediately clear whether it can explain the temporal variability that has been the primary focus of the present study. Seasonally, the subsurface poleward flow associated with topographic rectification is expected to be strongest when variability in the local wind stress is highest. In the northern CCS, the standard deviation of daily mean wind stress is strongest during December and reaches a minimum during August (Hickey 1979). Therefore, although topographic rectification cannot be ruled out as a potential mechanism, it does not appear to explain the intensification of poleward flow over the upper slope from spring to late summer.

The strength of the CUC also varies on interannual time scales, which may explain differences between seasonal averages of the NCOM-CCS results from 2005 and the Hickey (1979) current-meter observations from 1972 (section 3). Summer 1972 coincides with a strong El Niño, although it is not associated with significant warm temperature anomalies in the northern CCS like other El Niño years (Smith et al. 2001). However, current-meter measurements indicate much stronger poleward velocity over the outer shelf and slope during late summer 1972 than late summer 1981 (Hickey 1989). Mean late-summer poleward flow at 200 m over the upper slope is $\sim 0.05\text{ m s}^{-1}$ during 1981, compared with $\sim 0.15\text{ m s}^{-1}$ during 1972. Mean late-summer current-meter observations from 1981 show near-surface equatorward flow of about -0.20 m s^{-1} (Hickey 1989), compared with -0.08 m s^{-1} during the 1972 observations.

Over midshelf, at the 80-m isobath, late-summer observations from both 1972 and 1981 indicate that poleward flow extends throughout nearly the entire water column. However, neither observations nor model results show mean poleward flow in the midshelf water column during late summer 2005 (section 3). The presence of stronger equatorward flow over midshelf during 2005 than other years may be related to anomalous local wind stress, which transitioned equatorward about 1 month later than usual off the Washington coast but was stronger than usual during the later part of the summer (Hickey et al. 2006; Kosro et al. 2006). Sensitivity of alongshore currents to local wind stress in the CTW model is higher over the shelf than the slope (section 4a). It is therefore likely that interannual variability of the CUC in the northern CCS is more strongly influenced by remote forcing than local wind stress and also influenced by β -plane dynamics as discussed above.

The baroclinic structure of the APF presented in this study is consistent with the idealized model of McCreary (1981), in which the undercurrent deepens at higher latitudes and reaches a maximum amplitude at the latitude where isopycnal surfaces are shallowest (Fig. 11d). The presence of a poleward APF at depth over the slope does not depend on the southern boundary condition of the CTW model (Figs. 15b–c) or a strong poleward APF near the coast (Figs. 12a–c). McCreary and Chao (1985) show that this structure of the APF is robust even when the inclusion of a continental shelf weakens the undercurrent. The same basic structure is shown in the two-layer model of Yoshida (1967), in which the sea level reaches a minimum at the northern edge of the wind stress forcing and the shallowest depth of the thermocline occurs at the same latitude. In the present study, over the CA slope, the APF is poleward through the entire water column and alongshore density gradients weaken the poleward APF with depth (Figs. 11a–c), consistent with previous studies that focused on these latitudes (Mellor 1986; Pringle and Dever 2009).

Model hindcast results in the present study indicate that the largest vertical isopycnal displacements over the slope occur north of the strongest equatorward wind forcing (Fig. 11), in agreement with past idealized models (Yoshida 1967; McCreary 1981). Shipboard observations also suggest a maximum vertical isopycnal displacement over the slope that is offset to the north of the strongest upwelling-favorable winds (Muraki 1974). Vertical motions of isopycnals over the slope are associated with higher CTW modes, which are damped more quickly than the first-mode waves that dominate the coastal sea level response. Higher background stratification to the north may also contribute to the baroclinic APF by restricting the upward displacement of

isopycnals. In the CTW model, onshore flow associated with the poleward APF at the shelf break transfers mass from the poleward undercurrent to the equatorward shelf jet in the northern CCS. In NCOM-CCS, the baroclinic structure of the APF and associated cross-shore flow near the surface are complicated by the presence of equatorward flow farther offshore over the shelf break (Fig. 5). Observations have shown that the equatorward jet migrates offshore throughout the summer (Hickey 1989), which may influence the magnitude and structure of the poleward APF near the surface in the northern CCS. The contribution of density gradients to the poleward APF over the slope, demonstrated here in the northern CCS, is expected to be dynamically important in the poleward latitudes of other eastern boundary upwelling systems.

This study presents a comprehensive analysis of seasonal and event-scale flow over the continental slope of the CCS. Models are tested against a unique long-term dataset collected over the northern CCS slope. Our results highlight the importance of remote forcing in all parts of the CCS, which provides motivation for treating such systems as a unified whole in future modeling studies. The presence of strong variability at multiple time scales demonstrates that the collection of in situ data over the continental slope should be a critical component of future dynamical studies of poleward undercurrents in upwelling regions.

Acknowledgments. The authors thank Kenneth Brink (WHOI) for providing CTW software and Edward Dever (OSU) for providing RN mooring data. Ryan McCabe, Parker MacCready, Neil Banas, and two anonymous reviewers provided valuable feedback on earlier versions of the manuscript. I. Shulman thanks John Kindle, Sergio DeRada, Brad Penta, and Stephanie Anderson for help with NCOM-CCS. This work was part of T. Connolly's graduate research at the University of Washington and was supported by grants to B. Hickey from the Coastal Ocean Program of the National Oceanic and Atmospheric Administration (NOAA) (NA17OP2789 and NA09NOS4780180) and the National Science Foundation (NSF) (OCE0234587 and OCE0942675) as part of the Ecology of Harmful Algal Blooms Pacific Northwest (ECOHAB PNW) and Pacific Northwest Toxin (PNWTOX) projects. I. Shulman was supported by the Naval Research Laboratory. The statements, findings, conclusions, and recommendations are those of the authors and do not reflect the views of NSF, NOAA, or the Department of Commerce.

REFERENCES

- Atlas, R., R. N. Hoffman, J. Ardizzone, S. M. Leidner, J. C. Jusem, D. K. Smith, and D. Gombos, 2011: A cross-calibrated, multiplatform ocean surface wind velocity product for meteorological and oceanographic applications. *Bull. Amer. Meteor. Soc.*, **92**, 157–174.
- Bakun, A., and C. S. Nelson, 1991: The seasonal cycle of wind-stress curl in subtropical eastern boundary current regions. *J. Phys. Oceanogr.*, **21**, 1815–1834.
- Barron, C. N., A. B. Kara, H. E. Hurlburt, C. Rowley, and L. F. Smedstad, 2004: Sea surface height predictions from the global Navy Coastal Ocean Model during 1998–2001. *J. Atmos. Oceanic Technol.*, **21**, 1876–1893.
- Batteen, M. L., 1997: Wind-forced modeling studies of currents, meanders, and eddies in the California Current System. *J. Geophys. Res.*, **102** (C1), 985–1010.
- Battisti, D. S., and B. M. Hickey, 1984: Application of remote wind-forced coastal trapped wave theory to the Oregon and Washington coasts. *J. Phys. Oceanogr.*, **14**, 887–903.
- Boyer, T. P., and Coauthors, 2006: *World Ocean Database 2005*. U.S. Government Printing Office, 190 pp.
- Brink, K. H., 1989: Energy conservation in coastal-trapped wave calculations. *J. Phys. Oceanogr.*, **19**, 1011–1016.
- , 2010: Topographic rectification in a forced, dissipative, barotropic ocean. *J. Mar. Res.*, **68**, 337–368.
- , 2011: Topographic rectification in a stratified ocean. *J. Mar. Res.*, **69**, 483–499.
- , and D. C. Chapman, 1987: Programs for computing properties of coastal-trapped waves and wind-driven motions over the continental shelf and slope. 2nd ed. Woods Hole Oceanographic Institution Tech. Rep. WHOI-87-24, 119 pp.
- Castro, C. G., F. P. Chavez, and C. A. Collins, 2001: Role of the California Undercurrent in the export of denitrified waters from the eastern tropical North Pacific. *Global Biogeochem. Cycles*, **15**, 819–830.
- Chapman, D. C., 1987: Application of wind-forced, long, coastal-trapped wave theory along the California coast. *J. Geophys. Res.*, **92** (C2), 1798–1816.
- Clarke, A. J., and S. Van Gorder, 1986: A method for estimating wind-driven frictional, time-dependent, stratified shelf and slope water flow. *J. Phys. Oceanogr.*, **16**, 1013–1028.
- , and C. Shi, 1991: Critical frequencies at ocean boundaries. *J. Geophys. Res.*, **96** (C6), 10 731–10 738.
- Collins, C. A., L. M. Ivanov, and O. V. Mel'nichenko, 2003: Seasonal variability of the California Undercurrent: Statistical analysis based on the trajectories of floats with neutral buoyancy. *Phys. Oceanogr.*, **13**, 135–147.
- Csanady, G. T., 1978: The arrested topographic wave. *J. Phys. Oceanogr.*, **8**, 47–62.
- , 1985: "Pycnocathic" currents over the upper continental slope. *J. Phys. Oceanogr.*, **15**, 306–315.
- Emery, W. J., and R. E. Thomson, 2004: *Data Analysis Methods in Physical Oceanography*. 2nd ed. Elsevier, 638 pp.
- Federiuk, J., and J. S. Allen, 1995: Upwelling circulation on the Oregon continental shelf. Part II: Simulations and comparisons with observations. *J. Phys. Oceanogr.*, **25**, 1867–1889.
- Fox, D. N., W. J. Teague, C. N. Barron, M. R. Carnes, and C. M. Lee, 2002: The Modular Ocean Data Assimilation System (MODAS). *J. Atmos. Oceanic Technol.*, **19**, 240–252.
- Garfield, N., C. A. Collins, R. G. Paquette, and E. Carter, 1999: Lagrangian exploration of the California Undercurrent, 1992–95. *J. Phys. Oceanogr.*, **29**, 560–583.
- Haney, R. L., 1991: On the pressure gradient force over steep topography in sigma coordinate ocean models. *J. Phys. Oceanogr.*, **21**, 610–619.

- Hickey, B. M., 1979: The California Current System—Hypotheses and facts. *Prog. Oceanogr.*, **8**, 191–279.
- , 1989: Patterns and processes of circulation over the Washington continental shelf and slope. *Coastal Oceanography of Washington and Oregon*, M. R. Landry and B. M. Hickey, Eds., Elsevier, 41–115.
- , and N. E. Pola, 1983: The seasonal alongshore pressure gradient on the West Coast of the United States. *J. Geophys. Res.*, **88** (C12), 7623–7633.
- , R. E. Thomson, H. Yih, and P. H. LeBlond, 1991: Velocity and temperature fluctuations in a buoyancy-driven current off Vancouver Island. *J. Geophys. Res.*, **96** (C6), 10 507–10 538.
- , A. MacFadyen, W. Cochlan, R. Kudela, K. Bruland, and C. Trick, 2006: Evolution of chemical, biological, and physical water properties in the northern California Current in 2005: Remote or local wind forcing? *Geophys. Res. Lett.*, **33**, L22S02, doi:10.1029/2006GL026782.
- , and Coauthors, 2010: River influences on shelf ecosystems: Introduction and synthesis. *J. Geophys. Res.*, **115**, C00B17, doi:10.1029/2009JC005452.
- Hill, A. E., B. M. Hickey, F. A. Shillington, P. T. Strub, K. H. Brink, E. D. Barton, and A. C. Thomas, 1998: Eastern ocean boundaries. *The Sea: The Global Coastal Ocean*, A. R. Robinson and K. H. Brink, Eds., Vol. 11, *Regional Studies and Syntheses*, John Wiley and Sons, 29–67.
- Hodur, R. M., 1997: The Naval Research Laboratory's Coupled Ocean/Atmosphere Mesoscale Prediction System (COAMPS). *Mon. Wea. Rev.*, **125**, 1414–1430.
- Holloway, G., 1987: Systematic forcing of large-scale geophysical flows by eddy-topography interaction. *J. Fluid Mech.*, **184**, 463–476.
- Huthnance, J. M., 1984: Slope currents and JEBAR. *J. Phys. Oceanogr.*, **14**, 795–810.
- Huyer, A., J. A. Barth, P. M. Kosro, R. K. Shearman, and R. L. Smith, 1998: Upper-ocean water mass characteristics of the California Current, summer 1993. *Deep-Sea Res. II*, **45**, 1411–1442.
- Johnson, E. R., 1991: The scattering at low frequencies of coastally trapped waves. *J. Phys. Oceanogr.*, **21**, 913–932.
- Kelly, K. A., M. J. Caruso, and J. A. Austin, 1993: Wind-forced variations in sea surface height in the northeast Pacific Ocean. *J. Phys. Oceanogr.*, **23**, 2392–2411.
- Kosro, P. M., W. T. Peterson, B. M. Hickey, R. K. Shearman, and S. D. Pierce, 2006: Physical versus biological spring transition: 2005. *Geophys. Res. Lett.*, **33**, L22S03, doi:10.1029/2006GL027072.
- Large, W. G., and S. Pond, 1981: Open ocean momentum flux measurements in moderate to strong winds. *J. Phys. Oceanogr.*, **11**, 324–336.
- Lathuilière, C., V. Echevin, M. Lévy, and G. Madec, 2010: On the role of the mesoscale circulation on an idealized coastal upwelling ecosystem. *J. Geophys. Res.*, **115**, C09018, doi:10.1029/2009JC005827.
- Liu, K. K., and I. R. Kaplan, 1989: The eastern tropical Pacific as a source of ¹⁵N-enriched nitrate in seawater off southern California. *Limnol. Oceanogr.*, **34**, 820–830.
- MacFadyen, A., B. M. Hickey, and W. Cochlan, 2008: Influences of the Juan de Fuca Eddy on circulation, nutrients, and phytoplankton production in the northern California Current System. *J. Geophys. Res.*, **113**, C08008, doi:10.1029/2007JC004412.
- Marchesiello, P., J. C. McWilliams, and A. Shchepetkin, 2003: Equilibrium structure and dynamics of the California Current System. *J. Phys. Oceanogr.*, **33**, 753–783.
- McCreary, J. P., 1981: A linear stratified model of the coastal undercurrent. *Philos. Trans. Roy. Soc. London*, **A302**, 385–413.
- , and S.-Y. Chao, 1985: Three-dimensional shelf circulation along an eastern ocean boundary. *J. Mar. Res.*, **43**, 13–36.
- , P. K. Kundu, and S. Y. Chao, 1987: On the dynamics of the California Current System. *J. Mar. Res.*, **45**, 1–32.
- Mellor, G. L., 1986: Numerical simulation and analysis of the mean coastal circulation off California. *Cont. Shelf Res.*, **6**, 689–713.
- Muraki, H., 1974: Poleward shift of the coastal upwelling region off the California coast. *J. Oceanogr. Soc. Japan*, **30**, 49–53.
- Oey, L.-Y., 1999: A forcing mechanism for the poleward flow off the southern California coast. *J. Geophys. Res.*, **104** (C6), 13 529–13 539.
- Pares-Sierra, A., and J. J. O'Brien, 1989: The seasonal and interannual variability of the California Current System: A numerical model. *J. Geophys. Res.*, **94** (C3), 3159–3180.
- Pelland, N. A., C. C. Eriksen, and C. M. Lee, 2013: Subthermocline eddies over the Washington continental slope as observed by Seagliders, 2003–09. *J. Phys. Oceanogr.*, **43**, 2025–2053.
- Philander, S. G. H., and J.-H. Yoon, 1982: Eastern boundary currents and coastal upwelling. *J. Phys. Oceanogr.*, **12**, 862–879.
- Pierce, S. D., R. L. Smith, P. M. Kosro, J. A. Barth, and C. D. Wilson, 2000: Continuity of the poleward undercurrent along the eastern boundary of the mid-latitude North Pacific. *Deep-Sea Res.*, **47**, 811–829.
- Pringle, J. M., and E. P. Dever, 2009: Dynamics of wind-driven upwelling and relaxation between Monterey Bay and Point Arena: Local-, regional-, and gyre-scale controls. *J. Geophys. Res.*, **114**, C07003, doi:10.1029/2008JC005016.
- Reid, J. L., and A. W. Mantyla, 1976: The effect of the geostrophic flow upon coastal sea elevations in the northern North Pacific Ocean. *J. Geophys. Res.*, **81** (18), 3100–3110.
- Rhodes, R., and Coauthors, 2002: Navy real-time global modeling systems. *Oceanography*, **15**, 29–43.
- Shulman, I., and Coauthors, 2007: Modeling of upwelling/relaxation events with the Navy Coastal Ocean Model. *J. Geophys. Res.*, **112**, C06023, doi:10.1029/2006JC003946.
- , S. Anderson, C. Rowley, S. DeRada, J. Doyle, and S. Ramp, 2010: Comparisons of upwelling and relaxation events in the Monterey Bay area. *J. Geophys. Res.*, **115**, C06016, doi:10.1029/2009JC005483.
- Siedlecki, S. A., A. Mahadevan, and D. E. Archer, 2012: Mechanism for export of sediment-derived iron in an upwelling regime. *Geophys. Res. Lett.*, **39**, L03601, doi:10.1029/2011GL050366.
- Smith, R. L., A. Huyer, and J. Fleischbein, 2001: The coastal ocean off Oregon from 1961 to 2000: Is there evidence of climate change or only of Los Niños? *Prog. Oceanogr.*, **49**, 63–93.
- Suginohara, N., 1974: Onset of coastal upwelling in a two-layer ocean by wind stress with longshore variation. *J. Oceanogr.*, **30**, 23–33, doi:10.1007/BF02112888.
- , 1982: Coastal upwelling: Onshore–offshore circulation, equatorward coastal jet and poleward undercurrent over a continental shelf-slope. *J. Phys. Oceanogr.*, **12**, 272–284.
- , and Y. Kitamura, 1984: Long-term coastal upwelling over a continental shelf-slope. *J. Phys. Oceanogr.*, **14**, 1095–1104.
- Swartzman, G., B. Hickey, P. M. Kosro, and C. Wilson, 2005: Poleward and equatorward currents in the Pacific eastern boundary

- current in summer 1995 and 1998 and their relationship to the distribution of euphausiids. *Deep-Sea Res. II*, **52**, 73–88.
- Thomson, R. E., and M. V. Krassovski, 2010: Poleward reach of the California Undercurrent extension. *J. Geophys. Res.*, **115**, C09027, doi:10.1029/2010JC006280.
- Todd, R. E., D. L. Rudnick, M. R. Mazloff, R. E. Davis, and B. D. Cornuelle, 2011: Poleward flows in the southern California Current System: Glider observations and numerical simulation. *J. Geophys. Res.*, **116**, C02026, doi:10.1029/2010JC006536.
- Wang, D. P., and C. N. K. Mooers, 1976: Coastal-trapped waves in a continuously stratified ocean. *J. Phys. Oceanogr.*, **6**, 853–863.
- Werner, F. E., and B. M. Hickey, 1983: The role of a longshore pressure gradient in Pacific Northwest coastal dynamics. *J. Phys. Oceanogr.*, **13**, 395–410.
- Wilkin, J. L., and D. C. Chapman, 1990: Scattering of coastal-trapped waves by irregularities in coastline and topography. *J. Phys. Oceanogr.*, **20**, 396–421.
- Willmott, C. J., 1981: On the validation of models. *Phys. Geogr.*, **2**, 184–194.
- Yoshida, K., 1967: Circulation in the eastern tropical oceans with special references to upwelling and undercurrents. *Japanese J. Geophys.*, **4**, 1–75.
- , 1980: The coastal undercurrent—A role of longshore scales in coastal upwelling dynamics. *Prog. Oceanogr.*, **9**, 83–131.

Copyright of Journal of Physical Oceanography is the property of American Meteorological Society and its content may not be copied or emailed to multiple sites or posted to a listserv without the copyright holder's express written permission. However, users may print, download, or email articles for individual use.